Biomimetic Mn-Catalases Based on Dimeric Manganese Complexes in Mesoporous Silica for Potential Antioxidant Agent

Luis Escriche-Tur, [*,†,‡] Montserrat Corbella, [‡] Mercè Font-Bardia, [§] Isabel Castro, [‖] Laurent Bonneviot,[†] and Belén Albela [*,†]

† Laboratoire de Chimie, ENS de Lyon, Université de Lyon, 46 Allée d'Italie, 69364 Lyon Cedex 07, France
‡ Departament de Química Inorgànica and §Crystal·lografia, Mineralogia i Dipòsits Minerals, Universitat de Barcelona, 08028 Barcelona, Spain
‖ Institut de Ciència Molecular, Universitat de València, C/Catedrático José Beltrán 2, 46980 Paterna, Spain

ABSTRACT

Two new structural and functional models of the Mn-catalase with formula [{MnIII(bpy)(H2O)}(μ-2-MeOC6H4CO2)2(μ-O){MnIII(bpy)(X)}]X, where X = NO3 (1) and ClO4 (2) and bpy = 2,2′-bipyridine, were synthesized and characterized by X-ray diffraction. In both cases, a water molecule and an X ion occupy the monodentate positions. The magnetic properties of these compounds reveal a weak antiferromagnetic behavior (2J = −2.2 cm−1 for 1 and −0.7 cm−1 for 2, using the spin Hamiltonian H = −2J S1·S2) and negative zero-field splitting parameter DMn (−4.6 cm−1 and −3.0 cm−1 for 1 and 2, respectively). This fact, together with the nearly orthogonal orientation of the Jahn−Teller axes of the MnIII ions explain the unusual shape of χMT versus T plot at low temperature. Compound 1 presents a better catalase activity than 2 in CH3CN−H2O media, probably due to a beneficial interaction of the NO3 − ion with the Mn complex in solution. These compounds were successfully inserted inside twodimensional hexagonal mesoporous silica (MCM-41 type) leading to the same hybrid material ([Mn2O]@SiO2), without the X group. The manganese complex occupies approximately half of the available pore volume, keeping the silica's hexagonal array intact. Magnetic measurements of [Mn2O]@SiO2 suggest that most of the dinuclear unit is preserved, as a non-negligible interaction between Mn ions is still observed. The X-ray photoelectron spectroscopy analysis of the Mn 3s peak confirms that Mn remains as MnIII inside the silica. The catalase activity study of material [Mn2O]@SiO2 reveals that the complex is more active inside the porous silica, probably due to the surface silanolate groups of the pore wall. Moreover, the new material shows catalase activity in water media, while the coordination compounds are not active.

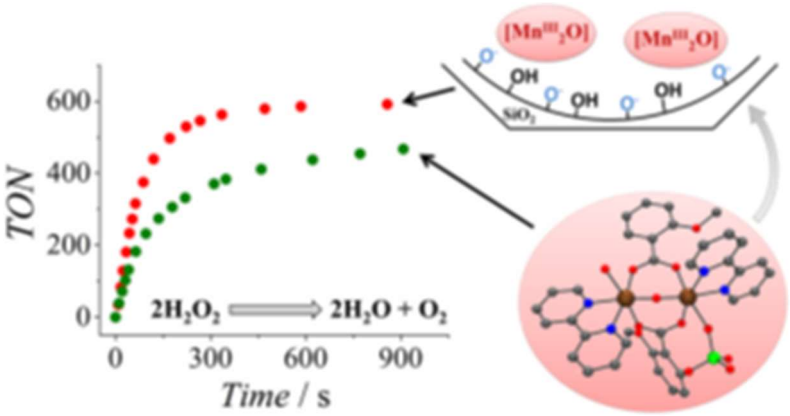

INTRODUCTION

Reactive oxygen species (ROS), represented by superoxide ($O_2^{\bullet-}$), hydrogen peroxide (H_2O_2), and hydroxyl radical ($HO^{\bullet}$), are endogenously produced in cells under aerobic conditions during the auto-oxidation of redox enzymes. ROS play an indispensable physiological role; however, their effects oppose one another as they can both promote and prevent cell death, inflammation, or aging.[1−3]

$O_2^{\bullet-}$ and H_2O_2 are produced from the one- and two-electron reduction of molecular oxygen (O_2), respectively. These two oxidants react rapidly with vulnerable targets; therefore, cells are loaded with high amounts of very efficient ROS scavengers, as, for example, catalase, peroxidases (H_2O_2 scavengers), or superoxide dismutases ($O_2^{\bullet-}$ scavengers). Consequently, a balance between the intracellular $O_2^{\bullet-}$ and H_2O_2 production and their scavenger-mediated decomposition keeps these two oxidants' concentration in steady-state. Whereas $O_2^{\bullet-}$ (small but charged) is not able to cross membranes, H_2O_2 (small and uncharged) crosses membranes at a moderate efficiency, making cells sensitive to the extracellular H_2O_2 concentration. Both $O_2^{\bullet-}$ and H_2O_2 are able to deteriorate the Fe_4S_4 clusters found in dehydratase enzymes, and, in the case of H_2O_2, this reaction leads to the formation of the hydroxyl radical ($HO^{\bullet}$), a process known as the Fenton reaction.[4] $HO^{\bullet}$ is an extremely powerful oxidant that, for instance, is responsible for direct DNA damage (since neither H_2O_2 nor $O_2^{\bullet-}$ are able to damage DNA directly).[2]

As with any signaling mechanism, ROS can become cytotoxic if found in high concentrations or in the wrong place. The phenomenon of ROS overproduction, which contributes to oxidative stress, has been found in a great number of pathologies[5−8] such as cancer, multiple sclerosis, Alzheimer's, or Parkinson diseases. Nevertheless, the role of ROS in such diseases is sometimes controversial since they may present various effects at the same time. For example, the production of ROS on tumors can range from tumor-production effects to tumor-destroying effects. In fact, some anticancer agents induce apoptosis, promoting the production of ROS, which contributes both to their efficacy and to their toxicity[3,9] (damaging tumor cells and noncancerous cells, which may cause sideeffects).

Owing to the harmful properties of ROS, antioxidant therapies have been considered for a wide variety of disorders associated with oxidative stress, which have shown promising in vivo results.[10−13] Unfortunately, clinical trials to test the effect of antioxidant therapies are limited and have presented disappointing results in lots of cases. Nevertheless, the use of improved antioxidant therapies is still considered nowadays in particular cases where the oxidative stress is shown in earlier stages before the development of severe clinical manifestations, such as in children with α-1 antitrypsin deficiency (characterized by H_2O_2 accumulation due to the lack of catalase activity).[14] Antioxidant therapy in combination with conventional therapies is also considered for diseases in which ROS play an important role in neuron-degeneration such as multiple sclerosis,[15,16] Alzheimer's,[17] or Parkinson's[18] syndromes. In these cases, the chosen antioxidants should be able to penetrate the blood-brain barrier, which is the major obstacle that reduces the efficacy of many agents.[15] Targeting antioxidants to the desired position opens a new challenge in molecular recognition, as oxidative stress is produced locally or is notably harmful for the most vulnerable targets. For instance, mitochondrially targeted antioxidants could effectively reduce oxidative stress in asthma.[19] Similarly, neonatal brain injury could be diminished or prevented by using antioxidants able to cross both the placenta and the blood-brain barrier.[20]

Within all antioxidants, catalases (CATs) are the enzymes that perform the decomposition of H_2O_2 into H_2O and O_2. In particular, Mn-CATs are found in some lactic acid bacteria. The active site of this type of CATs comprises a dinuclear Mn unit with oxo and carboxylate bridges, in which the oxidation states in the Mn_2 pair alternate between (II,II) and (III,III).[21] Efforts to mimic the active site and the catalytic performance of this enzyme have been performed. A large number of functional models of the Mn-CAT

were summarized in 2012 by Signorella and Hureau.22 More recently, mononuclear MnIII porphyrin, Schiff-base, and salen complexes have received much devotion23−27 and have deflected the attention from MnIII2 mimics, reducing the emergence of this latter type.28 Moreover, dinuclear models with the required stability and activity in physiological conditions have not been reported so far. The insertion of Mn-CAT model compounds in porous solids offers the possibility of mimicking different properties found in the native catalytic site, such as hydrophobicity and confinement.29−32 Indeed, the encapsulation of antioxidants into nanocarriers could provide not only an improvement of stability but also a higher therapy efficiency.33 Among inorganic-based materials, mesoporous silicas have attracted much attention because of their biocompatibility at practical concentrations and their ability to protect pharmaceutical principles from premature release or undesired degradation in living systems, acting as an effective drug delivery system. Moreover, the versatile control over the internal and external surface functionalization is advantageous for the adaptability to any guest environment .34

With this frame, we present here the synthesis of two new model compounds of the Mn-CAT's active site with formula [{MnIII(bpy)(H2O)}(μ-2-MeOC6H4CO2)2(μ-O){MnIII(bpy)-(X)}]X, where X = NO3 (1) and ClO4 (2) and bpy = 2,2′- bipyridine, and their characterization with single-crystal X-ray diffraction. This kind of compounds is interesting from the magnetic point of view due to the effect of the structural parameters on the type and intensity of the magnetic interaction; as we have reported previously, these systems could show different ground-spin state (S = 0 or S = 4).35−37 In this work we analyze the magnetic interaction and the influence of the anisotropy in the magnetic behavior. Moreover, we report here the catalase activity of these compounds.

With the aim to mimic the cavity of the Mn-CAT enzyme, the two coordination compounds 1 and 2 were inserted in the nanochannels of mesoporous silica (MCM-41 type), and the resulting materials [Mn2O]@SiO2 were characterized. The catalase activity of this new material is compared with that shown by 1 and 2 to eventually evidence the advantages of the latter over the former. The reactivity is run in a mixture of acetonitrile−water and pure water.

EXPERIMENTAL SECTION

Synthesis of the Manganese(III) Compounds. All manipulations were performed at room temperature under aerobic conditions. Reagents and solvents were obtained from commercial sources and used without further purification. NBu_4MnO_4 was prepared as described in the literature.38 Caution! Perchlorate salts of compounds containing organic ligands are potentially explosive. Only small quantities should be prepared.

[{Mn(bpy)(H_2O)}(μ-2-$MeOC_6H_4CO_2$)$_2$(μ-O){Mn(bpy)(NO_3)}]NO_3 (1). 2-$MeOC_6H_4COOH$ (0.24 g, 1.6 mmol), previously dissolved in acetonitrile, was added to a solution of Mn(NO_3)·4H_2O (0.32 g, 1.28 mmol). An acetonitrile solution of NBu_4MnO_4 (0.12 g, 0.32 mmol) was added to the previous mixture in small portions during 1−2 min, while, almost simultaneously, 10 mL of acetonitrile solution of 2,2′- bipyridine (bpy; 0.25 g, 1.6 mmol) was added, also in small portions. The resulting black solution (total volume ≈ 60 mL) was stirred for 15 min and shortly afterward filtered to separate a dark precipitate. Dark crystals were isolated by filtration after 6 d of slow evaporation at room temperature, washed with ether, and dried under vacuum. Yield: 40%. X-ray quality single-crystals were obtained by very slow evaporation of the mother solution after 15 d. Anal. Calcd for $C_{36}H_{32}Mn_2N_6O_{14}$· 2$H_2O$ (%): C, 47.07; H, 3.95; N, 9.15. Found (%): C, 46.04; H, 3.88; N, 9.13. Selected IR data (cm−1): 3409 (br), 3093 (w), 3058 (w), 3031 (w), 2970 (w), 1601 (s), 1565 (m), 1498 (w), 1488 (m), 1449 (m), 1359 (s), 1294 (w), 1276 (w), 1245 (m) 1177 (w), 1162 (w), 1147 (w), 1102 (w), 1033 (m), 1021(w), 844 (w), 765 (s), 729 (m), 661 (m), 536 (w), 463 (w).

[{Mn(bpy)(H_2O)}(μ-2-$MeOC_6H_4CO_2$)$_2$(μ-O){Mn(bpy)(ClO_4)}]ClO_4 (2). An analogous procedure was followed as for 1, but using Mn(ClO_4)$_2$·6H_2O (0.46 g, 1.28 mmol) and only 30 mL of acetonitrile. Dark crystals were isolated after 10 d of slow evaporation at room temperature. Yield: 60%. Very thin single crystals were obtained by leaving the solution undisturbed in the refrigerator after one month. Anal. Calcd for $C_{36}H_{32}Cl_2Mn_2N_4O_{16}$·0.25$CH_3CN$ (%): C, 45.30; H, 3.35; N, 6.15; Cl, 7.33. Found (%): C, 45.10; H, 3.35; N, 6.13; Cl, 7.33. Selected IR data (cm−1): IR (cm−1): 3419 (br), 3093 (w), 3084 (w), 3013 (w), 2973 (w), 2839 (w), 1602 (s), 1561 (s), 1497 (w), 1471 (m), 1448 (m), 1377 (s), 1322 (w), 1280 (w), 1247 (m), 1107 (s,br), 1032 (m), 848 (w), 762 (s), 730 (m), 663 (m), 625 (m), 573 (w), 475 (w), 415 (w).

Synthesis of [Mn_2O]@SiO_2. The manganese complex was inserted into LUS mesoporous silica29,39 by ionic exchange using a masking agent as described elsewhere.40 The mesoporous silica was prepared as explained below, following the ultrafast microwave-assisted synthesis reported by J. Chaignon et al.41

Sodium Silicate Solution. Ludox HS-40 (187 mL, 1.6 mol SiO_2) was added to a sodium hydroxide (32 g, 0.80 mol) in 800 mL of distilled water and then stirred at 40 °C overnight until obtaining a colorless solution.

SiO_2−CTA. Cetyltrimethylammonium tosylate (CTATos; 7.84 g, 17 mmol) was stirred in water (284 mL) at 60 °C until its complete dissolution. Meanwhile, the sodium silicate solution previously prepared (196 mL) was also stirred at 60 °C for 1 h and then added to the surfactant one by pouring it slowly on the edge of the recipient. After a vigorous shaking by hand, the resulting white mixture was placed in several autoclaves and heated in a Berghof speedwave oven. It provides a microwave irradiation at 2450 MHz with a power of 1450 W. The experimental conditions used were: T = 180 °C, ramp = 1 min, plateau = 9 min (total heating time = 10 min). The autoclaves were allowed to cool at room temperature. Then, a white solid was filtered, washed with distilled water (∼500 mL), and dried at 80 °C to obtain 13.00 g of SiO_2−CTA. Anal. Calcd for SiO_2·0.13 CTA·0.40 H_2O (%): C, 28.45; H, 6.05; N, 1.75. Found: C, 28.75; H, 5.95; N, 1.72; S, 0.00. Residual mass at 1100 °C (%): 55.43. SiO_2−Ex. The surfactant was extracted by stirring SiO_2−CTA (300 mg) and HCl 1 M (0.75 mL) in technical ethanol

(60 mL) during 1 h. Then, the solid was filtered, washed twice with technical ethanol (20 mL), and dried overnight at 80 °C.

SiO2−TMA. Tetramethylammonium bromide (TMABr; 7.08 g, 45 mmol) was stirred with ethanol 70% (600 mL) at 40 °C for 1 h. Then, SiO2−CTA (12.5 g) was added to the previous solution, and the resulting suspension was stirred at 40 °C for 1 h. A white solid was separated by filtration and washed twice with ethanol 70% (200 mL) and acetone (200 mL). This procedure was repeated three times to ensure an entire exchange of the surfactant. Finally, the solid was dried at 80 °C to obtain 8.42 g of product. Anal. Calcd for SiO2·0.105 TMA· 0.35 H2O (%): C, 6.80; H, 2.66; N, 1.98. Found: C, 7.03; H, 2.61; N, 1.93. Residual mass at 1100 °C (%): 81.23.

[Mn2O]@SiO2. SiO2−TMA (0.5 g) was pretreated at 130 °C under vacuum for 1 h and then allowed to cool to room temperature. Meanwhile, compound 1 (250 mg, 0.272 mmol) was stirred for 1 h in acetonitrile (75 mL). Then, the dark brown manganese solution was slowly added over SiO2−TMA and stirred for 24 h. The resulting brown suspension was filtered, obtaining a dark brown powder and a clear brown solution. The powder was washed twice with acetonitrile (20 mL) and dried at 80 °C overnight to obtain 0.51 g of solid. Anal. Calcd for SiO2·0.033 [Mn2O(2-MeOC6H4CO2)2(bpy)2]·0.005 TMA· 0.35 H2O (%): C, 15.91; H, 1.93; N, 2.10; Si, 30.80; Mn, 3.98. Found: C, 15.85; H, 1.95; N, 2.08; Si, 30.80; Mn, 3.98; Cl, 0.00. Residual mass at 1100 °C (%): 72.04. The same procedure was performed but using compound 2 (251 mg, 0.272 mmol), and a solid with the same characteristics was obtained. Elemental analyses found (%): C, 15.79; H, 1.87; N, 2.01; Cl, 0.00. Residual mass at 1100 °C (%): 70.84.

Single-Crystal X-ray Crystallography. Crystallographic data collection and structure refinement details are summarized in Table 1. The data collection for compound 1 was performed at 100 K on a Bruker Apex-II diffractometer with a graphite monochromatic Mo Kα radiation (λ = 0.710 73 Å). Unit-cell parameters were determined from 9988 reflections (2.39 < θ < 25.06°) and refined by least-squares method. Data (27952 reflections) were collected (2.39 < θ < 25.08°) using the ω and Φ scan method and corrected for absorption effects using multiscan method (SADABS).42

The data collection for compound 2 was performed at 100 K on a D8 VENTURE diffractometer with a graphite monochromated Mo Kα radiation (λ = 0.710 73 Å). Unit-cell parameters were determined from 983 reflections (2.99 < θ < 19.65°) and refined by least-squares method. Data (4226 reflections) were collected (1.15 < θ < 20.81°) using the ω and Φ scan method and corrected for absorption effects using empirical method (SADABS).42

The structures were solved by direct methods and refined by fullmatrix least-squares using SHELXL-97.43 Non-hydrogen atoms were refined anisotropically, whereas hydrogen atoms were computed and refined with isotropic thermal parameters riding on their respective carbon or oxygen atoms.

Compound 1·H2O·0.5 CH3CN crystallizes in monoclinic space group C2/c. In the asymmetric unit, only half a cationic complex [{Mn(bpy)(H2O)0.5(NO3)0.5}2(μ-2-MeOC6H4CO2)2(μ-O)]+ may be found. The other half is generated by a twofold axis. The voids between complexes are filled by one molecule of disordered nitrate ion per molecule of complex and disordered solvent (water and acetonitrile). A total of 306 parameters were refined in the final refinement on F2 using 106 restraints.

Compound 2·CH3CN crystallizes in monoclinic space group P21/c. The asymmetric unit consists of a cationic complex [{Mn(bpy)-(H2O)}(μ-2-MeOC6H4CO2)2(μ-O){Mn(bpy)(ClO4)}]+, a perchlorate ion, and an acetonitrile molecule. A total of 562 parameters were refined in the final refinement on F2 using only one restraint. The isolated crystals of compound 2 were very thin (0.02 mm thickness), being poorly diffracting at high angles. Other attempts of crystallization were done, but no single crystals of better quality were obtained. Nevertheless, the absence of disorder and the simplicity of the crystal structure made us able to refine the crystal structure without any trouble.

Physical Characterization. Chemical analyses (C, H, N, and Cl) were performed by the "Centres Cientifí cs i Tecnologì ics" of the Universitat de Barcelona and by the "Servei de Microanàlisi" of the "Consell Superior d'Investigacions Cientifí ques" (CSIC). Inductively coupled plasma optical emission spectrometry (ICP-OES) was performed to determine Mn and Si percentages by the "Centres Cientifí cs i Tecnologì ics" of the Universitat de Barcelona from a solution of material [Mn2O]@SiO2 (~20 mg) pretreated at 90 °C with a mixture of HF (200 μL) and HNO3 (1 mL) into an autoclave. Infrared spectra were recorded on KBr pellets in the 4000−400 cm−1 range with a Thermo Nicolet Avatar 330 FTIR spectrometer. Thermogravimetric analysis (TGA) was performed with a NETZSCH STA 409 PC Luxx device under aerobic conditions with a 10 °C/min temperature increase. Nitrogen sorption isotherms at 77 K were determined with a volume device Belsorp Marx on solids that were dried under vacuum overnight at 130 °C (samples SiO2−Ex and SiO2−TMA) or at 80 °C (samples [Mn2O]@SiO2, [Mn2O]@SiO2 #A, [Mn2O]@SiO2 #W, and [Mn2O]@SiO2 #M). Low-angle X-ray powder diffraction (XRD) was performed using a Bruker (Siemens) D5005 diffractometer with Cu Kα monochromatic radiation. Transmission electron microscopy (TEM) analysis was performed with a TOPCON Em-002b and operated at 120 kV, dispersing material [Mn2O]@SiO2 in ethanol and depositing it on a Holey carbon 300 mesh copper grid. The ionic conductivity (Λ) measurements were made on a 0.8 mM acetonitrile solution of compound 1 and 2 using a CDC401 electrode. Magnetic susceptibility (χM) measurements (2−300 K) were performed in a Quantum Design MPMS XL5 SQUID Magnometer at the Unitat de Mesures Magnètiques of the University of Barcelona. Two different magnetic fields were used for the susceptibility measurements, 0.02 T (2−29 K) and 0.3 T (2−300 K), with imposable graphs. Magnetization isotherms measurements were made in the range 1.8−6.8 K and at six different magnetic fields (0.5, 1.0, 2.0, 3.0, 4.0, 5.0 T). Pascal's constants were used to estimate the diamagnetic corrections for compounds 1 and 2 and material [Mn2O] @SiO2. The fit was performed by minimizing functions RSUS = Σ[(χMT)exp − (χMT)calcd]2/Σ[(χMT)exp]2 and RMAG = Σ[(M/Nμβ)exp − (M/Nμβ)calcd]2/Σ[(M/Nμβ)exp]2. Electron paramagnetic resonance (EPR) spectra were recorded at X-band (9.4 GHz) frequency using a Bruker ESP-300E spectrometer, from room temperature to 20 K at the Unitat de Mesures Magnètiques (Universitat de Barcelona).

X-ray Absorption Spectroscopy. X-ray absorption near edge structure (XANES) of well-pounded microcrystalline powders of homogeneous thickness and calculated weight samples of compound 1 and material [Mn2O]@SiO2 were collected at room temperature at the synchrotron ALBA in Barcelona (Spain) on the BL22 (CLÆSS) beamline. The measurements were performed at the Mn K-edge in the transmission mode. The experiments were calibrated by verifying that the first inflection point in all manganese foil spectra recorded together with XANES spectra of the compounds was 6539 eV.

X-ray Photoelectron Spectroscopy. XPS experiments were performed in a PHI 5500 Multitechnique System (from Physical Electronics) with a monochromatic X-ray source (Al Kα line of 1486.6 eV energy and 350 W), placed perpendicular to the analyzer axis and calibrated using the 3d5/2 line of Ag with a full width at half-maximum of 0.8 eV. The analyzed area was a circle of 0.8 mm diameter, and the selected resolution for the spectra was 187.85 eV of pass energy and 0.8 electronvolts per step for the general spectra and 23.5 eV of pass energy and 0.1 electronvolts per step for the spectra of the different elements. A low-energy electron gun (less than 10 eV) was used to discharge the surface when necessary. All measurements were made in an ultrahigh vacuum chamber pressure between 5 × 10−9 and 2 × 10−8 Torr. Binding energies were further referenced to the Csp2 peak at 284.6 eV.

Catalase Activity. The study of the catalase activity (H2O2 decomposition into H2O and O2) was performed at 25 °C by volumetric determination of the oxygen evolved with a gas-volumetric buret (precision of 0.1 mL). A 32% H2O2 aqueous solution (0.6 mL) was added to closed vessels containing acetonitrile solutions or suspensions of compounds 1 or 2 or material [Mn2O]@SiO2 (5 mL, 0.8 mM referred to Mn2 unit), and the oxygen evolved was volumetrically measured. It is worth emphasizing that the catalase activity was studied in a CH3CN−H2O 9:1 (v/v) (5 mL of CH3CN with the complex or the material and 0.6 mL of H2O2 aqueous solution). The same procedure was repeated with the three

systems (compounds 1 or 2 or material [Mn2O]@SiO2) using pure water as solvent instead of CH3CN. Blank experiments performed without the catalyst (in both solvents) showed a negligible disproportionation of H2O2. The catalytic activity of Mn(NO3)2 and MnO2 toward H2O2 disproportion was tested under the same conditions as those used for 1 and 2 with H2O2 (0.6 mL) at 32% and a 1.6 mM acetonitrile solution (5 mL), equivalent to [Mn2] = 0.8 mM.

The pH measurements were made using a PHC10101 electrode. As the electrode was calibrated in water, the pH measured in CH3CN−H2O 9:1 (v/v) (w s pH) was converted to s s pH (pH measured in CH3CN−H2O with electrodes calibrated in the same mixture) using the δ conversion parameter as described by L. G. Gagliardi et al.44 The following equation was used: s s pH = w s pH − δ, where δ = −1.61 at 20 °C. The pH values given in this work correspond to s s pH.

The pH-dependence study in the catalase activity was performed for compound 2. The evolution of oxygen was measured at different pH values using the same method and under the same conditions. Et3N 99% was used to increase the initial pH of the reaction media, yielding s s pH = 7.3, 9.8, 10.7, 11.8, and 12.0, for Et3N concentrations of 1.3, 2.5, 3.8, 12.6, and 19.0 mM, respectively.

Material [Mn2O]@SiO2 (22 mg) was dispersed in CH3CN (10 mL), leading to [MnIII 2] = 0.8 mM. Then, H2O2 32% (1.2 mL) was added ([H2O2]0 = 1.05 M). Several fractions (of ∼0.6 mL) of this suspension were filtered at 30, 90, 230, and 600 s and 2 h after the addition of H2O2. Then, EPR spectra of the filtered solutions were recorded at room temperature. The EPR calibration was performed using manganese(II) perchlorate ([MnII] = 0.044−1.45 mM) .

The solid separated at 90 s after the addition of H2O2 in the previous experiment was washed as soon as possible with CH3CN (20 mL) and analyzed by EPR and XPS.

Postcatalysis Products. [Mn2O]@SiO2 #A. [Mn2O]@SiO2 (100 mg) was stirred in acetonitrile (63 mL) for 1 or 2 min. Then, a 32% H2O2 aqueous solution (7.5 mL) was added, causing immediate vigorous evolution of O2. After 2 h, the brown solid was separated by filtration and dried overnight at 80 °C.

[Mn2O]@SiO2 #W. An analogous procedure was followed as for [Mn2O]@SiO2 #A, but using distilled water instead of acetonitrile.

Stability in Water. [Mn2O]@SiO2 #M. [Mn2O]@SiO2 (24 mg) was stirred in H2O (15 mL) for 2 h. The brown solid was separated by filtration, washed with H2O (20 mL), and dried overnight at 80 °C.

RESULTS AND DISCUSSION

Synthesis of Mn(III) Compounds: [{Mn(bpy)(H2O)}(μ-2-MeOC6H4CO2)2(μ-O){Mn(bpy)(X)}]X. Two binuclear Mn(III) compounds were obtained from the comproportionation reaction between MnX2 (X = NO3 or ClO4) and NBu4MnO4 in the presence of 2-MeOC6H4COOH and 2,2′-bipyridine, which leads to compounds with general formula [{Mn(bpy)-(H2O)}(μ-2-MeOC6H4CO2)2(μ-O){Mn(bpy)(X)}]X. The stoichiometry of this reaction is

1.6MnX2 + 2(2 – MeOC6H4 COOH) + 0.4NBu4 MnO4 + 2bpy → [{Mn(bpy)(H2O)}(μ - 2 - MeOC6H4CO2)2 (μ- O){Mn(bpy)(X)}]X + 0.4NBu4X + 0.8HX + nH2O

IR spectra of these compounds show two characteristic bands at ∼1560 and 1365 cm−1, corresponding to the asymmetric and symmetric vibrations of the carboxylate groups, respectively. The bands centered at ∼1600, 1498, 1480, and 1450 cm−1 are assigned to the bipyridine. The Mn−O−Mn group displays a moderate band at ∼730 cm−1. The spectrum of compound 1 exhibits an intense band at 1352 cm−1 corresponding to the nitrate anion, which overlaps the vs(COO). In the spectrum of compound 2, an intense band at 1120 cm−1 and a moderate band at 623 cm−1 are observed, being assigned to the perchlorate anion.

Description of the Structures. Figures 1 and 2 show the crystal structures of 1 and 2, respectively. As can be seen, both compounds display similar structures. The Mn(III) ions exhibit a distorted octahedral environment and are linked one to another by one oxo and two μ1,3-2-methoxybenzoate bridges. Each manganese ion is bound to a 2,2′-bipyridine ligand. The hexacoordination of each Mn ion is completed by a monodentate ligand.

The structural parameters of compounds 1 and 2 are in agreement with those reported for compounds with the same [Mn2(μ-O)(μ-2-RC6H4CO2)2]2+ core.35−37 Selected interatomic distances are listed in Table 2 and Table 3. The Mn···Mn distance is ∼3.15 Å, and the Mn−O−Mn angle is ∼123°. The Mn−O bond distances of the oxo bridges are ∼1.78 Å, and the Mn−N distances are ∼2.06 Å. The Mn−O bond lengths of the monodentate ligands are the largest ones in the first coordination sphere, being in the range of 2.17−2.38 Å, depending on the monodentate ligand. The carboxylate ligands are coordinated in a syn−syn mode. One of the oxygen atoms is placed trans to the monodentate ligand, with Mn−O distances of ∼2.16 Å, whereas the other oxygen atom is trans to a nitrogen atom of the bpy ligand, with a shorter Mn−O distance (∼1.96 Å).

[{Mn(bpy)(H2O)}(μ-2-MeOC6H4CO2)2(μ-O){Mn(bpy)-(NO3)}]NO3·H2O·0.5CH3CN (1·H2O·0.5CH3CN). The crystal structure of compound 1 consists of a cationic complex, a nitrate ion, and disordered solvent. The structure of its cationic complex is shown in Figure 1. The Mn ions display an elongated coordination environment toward the monodentate ligand direction due to the Jahn−Teller effect. The relative orientation of the manganese octahedra is far from being perpendicular, with an O5−Mn1−Mn1′−O6′ torsion angle of 78.1°. The aromatic ring and the carboxylate group of the 2-methoxybenzoate ligand are not coplanar with respect to an O3−C11−C12−C13 torsion angle of 36.2°.

The monodentate ligands of Mn(III) ions are disordered, being H2O or NO3−, both found with 50% occupancy. Therefore, the two Mn(III) ions that form the complex are crystallographically equivalent. Each binuclear entity is connected to the neighbor through hydrogen bonds between a H2O molecule and a NO3 − ion (Figure S1). This interaction is extended along a longitudinal axis, resulting in a monodimensional supramolecular structure, where the position of the H2O molecule and the NO3

− ion within each aforementioned couple is statistically dictated (Figure S1). Different longitudinal organizations are aligned in a zigzag layer where every chain is antiparallel to the previous one (Figure S2). A paralleldisplaced π−π interaction may be found between bipyridine ligands of adjacent chains (Figure S1). Finally, the resulting layers are antiparallel stacked, giving place to channels that are filled with anion and solvent molecules, both of them highly disordered (Figure S2).

[{Mn(bpy)(H2O)}(μ-2-MeOC6H4CO2)2(μ-O){Mn(bpy)-(ClO4)}]ClO4·CH3CN (2·CH3CN). The crystal structure of compound 2 consists of a cationic complex, a perchlorate ion, and an acetonitrile molecule. The structure of its cationic complex is shown in Figure 2. In this case, the two Mn(III) ions are not equivalent, having not only slightly different structural parameters but also different monodentate ligands. These two ions also display an elongated coordination environment toward the direction of such ligand. A water molecule is coordinated to Mn1 atom, with a Mn1−O8 distance of 2.219 Å, whereas a perchlorate ion is bound to Mn2 atom, the Mn2−O9 distance being 2.300 Å. As may be noticed, the Mn−O bond length is significantly larger when the ClO4 − ion is the monodentate ligand, as reported previously.36 The relative orientation of the manganese octahedra is closer to being perpendicular than in compound 1, having an O8−Mn1··· Mn2−O9 torsion angle of 95.2°. The 2-methoxybenzoato ligand, which is trans to the ClO4 − ion, is closer to planarity than the one that is trans to the H2O molecule, as indicated by the O5−C29−C30−C35 and O2−C21−C22−C27 torsion angles, which are 50.3 and 8°, respectively.

The binuclear complexes are connected through the noncoordinated perchlorate anions, which are bound to the water ligand via hydrogen bonds, being extended as a zigzag chain (Figure S3). No interaction is found between different chains. This chainlike structure is also found in an analogous compound reported by V. Gómez et al.36

Magnetic Properties. Magnetic susceptibility (χM) data were recorded for compounds 1 and 2 from 300 to 2 K. χMT versus T plots for 1 and 2 are shown in Figure 3. The χMT values at room temperature are close to 6.0 cm3·mol−1·K, which is the expected value for two uncoupled MnIII ions. χMT remains constant until 100 K; below this temperature it decreases to 2.2 (1) and 3.2 (2) cm3·mol−1·K at 2 K. This behavior is indicative of a weak antiferromagnetic coupling (ground state with S = 0). Magnetization (M) data were collected in the range of 1.8−6.8 K using six different values of the magnetic field (0.5−5.0 T), and M/Nμβ versus HT plots for compound 1 and 2 are shown in Figure S4 and Figure 3 (inset), respectively. The nonsuperposition of the various iso-field lines is indicative of a significant zero field splitting (ZFS). Both plots present a similar feature, but the M/Nμβ values tend to ∼4.2 for compound 1, whereas those same values tend to ∼5.5 for 2.

These compounds show an unusual behavior at low temperatures since χMT values do not tend to zero, as expected for an S = 0 ground state. To fit the whole curve, we took into account the zero-field splittings (ZFS) DMn and EMn, which are related to the axial and rhombic anisotropy of the MnIII octahedra, respectively. This effect splits the S states into the MS components. The resulting separation and organization of these MS states (DS and ES) depend on the magnitudes, signs, and directionalities of DMn and EMn.45 In the case of a weak antiferromagnetic system like ours, the excited states S = 1 and S = 2 are populated at low temperature, and the states |1, ± 1⟩, | 2, ± 2⟩, and |2, ± 1⟩ could be more relevant than the respective states |1, 0⟩ and |2, 0⟩ for negative values of DS=1 and DS=2. This fact could explain the deviation of the χMT plot in the lowtemperature range.

Therefore, χMT versus T and M/Nμβ versus HT data were fitted simultaneously using the PHI program (H = −2JS1S2),46 considering the ZFS of manganese(III) ions (DMn and EMn) and a relative orientation of the Jahn−Teller axes of 90°. For compound 1, the best fit corresponds to g = 2.01, 2J = −2.2 cm−1, DMn = −4.6 cm−1, and EMn (kept constant) = 1.0 cm−1 with RSUS = 5.5 × 10−5 and RMAG = 2.9 × 10−3. The EMn/DMn ratio is ∼0.2, in agreement with the rhombic distortion of the MnIII octahedra.47,48 For 2, the best fit corresponds to g = 2.01, 2J = −0.7 cm−1, and DMn = −3.0 cm−1, with RSUS = 9.0 × 10−5 and RMAG = 1.1 × 10−3 (see definition of RSUS and RMAG in

Experimental Section). In this case, considering EMn was unnecessary to achieve a good fit of the experimental data. The difference in the magnitude of the magnetic interaction between these complexes could be rationalized with their structural parameters (elongation parameter λ and the relative orientation of the octahedra τ) as it was previously reported by V. Gómez et al.36 As commented above, compound 2 displays a greater elongation in the direction of the monodentate ligand (with $\lambda > 2$) than 1 (with $\lambda < 2$); thus, a more antiferromagnetic interaction was expected for 2. However, the magnetic interaction for 2 is very weak, and the one for 1 is more antiferromagnetic than the expected considering only the distortion around the Mn(III) ions. This behavior could be explained with the relative disposition of the octahedra being more antiferromagnetic the lower the τ angle is. Indeed, 1 has a relatively high τ angle (O8−Mn1···Mn2−O9 angle of 95.2°), whereas 2 has the lowest τ angle found so far for this kind of compound (O5−Mn1···Mn1′−O6′ angle of 78.1°). So, the magnetic properties of these compounds are in agreement with the magnetostructural correlations reported previously.36 The values obtained for DMn are also consistent for MnIII ions with elongated octahedral geometry, which is expected to be moderate (between −2.3 and −4.5 cm−1) and negative.47−50

In conclusion, compounds 1 and 2 present moderate DMn values, and because of their weak magnetic interactions and low |J| values, the anisotropy of MnIII ions is more important than expected for antiferromagnetic compounds. Therefore, the $MS \neq 0$ states are relevant due to the sign of DMn and the relative orientation of the Jahn−Teller axes, affecting the shape of χMT versus T plot.

Insertion of Mn(III) Compounds into Mesoporous Silica: [Mn2O]@SiO2. Synthesis Strategy. Cationic complexes of compounds 1 and 2 were inserted into the nanopores of mesoporous silica by ionic exchange.40 A step-by-step procedure to obtain material [Mn2O]@SiO2 is shown in Figure 4. Two-dimensional (2D) hexagonal LUS silica (MCM−41 type), prepared at high temperature using CTATos as a surfactant, was chosen as a support.29−32 It possesses a large pore volume of 0.80 ± 0.01 cm3·g−1 and a narrow pore size distribution (pore diameter = 3.8 ± 0.1 nm) that may be suitable for the insertion of compounds 1 and 2, which are ∼1.3 nm wide. The cationic surfactant of the as-made silica (SiO2− CTA) was exchanged for tetramethylammonium cations (TMA+) using the procedure described by K. Zhang et al.,40 leading to the formation of SiO2−TMA with molar composition SiO2·0.105 TMA·0.35 H2O.

[Mn2O]@SiO2 was prepared from the mixture of an acetonitrile solution of compound 1 or 2 and SiO2−TMA at room temperature. TMA+, which is only held into the silica by electrostatic forces, is easily displaced when other positively charged species with more affinity for silica are present. The [Mn2]2+/TMA+ molar ratio used was 0.5, which corresponds to 1.0 for charge ratio.

The elemental analysis revealed that materials [Mn2O]@ SiO2 obtained from 1 or 2 have the same molar composition, and their IR spectra were superimposable. The results obtained from thermogravimetric analysis as well as from N2 sorption isotherms for both materials may be considered identical (Table 4 and Figure S5), as the differences between the solids are within the experimental error. These facts prove that the counteranions have an unperceived effect and, obviously, that they remain in solution without being retained by the silica.

Morphology of the Hybrid Material. The hexagonal array of the internal pores of the material was unaltered during the insertion of the Mn complex, as shown from the XRD patterns (Figure S6; the distance between the centers of the pores (a0) being 4.8 ± 0.1 nm (Table 4)). The TEM images of the hybrid material [Mn2O]@SiO2 (Figure S7) confirm the persistence of the cylinder array along the (110) plane. The low-temperature nitrogen sorption isotherms of the surfactant-extracted support, SiO2−Ex, and the hybrid solids, SiO2−TMA and [Mn2O]@ SiO2, exhibit a type IV isotherm according to the IUPAC nomenclature, without hysteresis as usually observed for MCM- 41 2D hexagonal mesoporous silica.30,51 The decrease of pore volume from 0.80 to 0.36 cm3·g−1 after the insertion confirms the presence of the complex inside the pores. This is also consistent with the decrease of intensity of the peak (100) observed in XRD of material [Mn2O]@SiO2, since a lower intensity is expected for those

whose contrast between silica wall and the channel atom occupancy is lower.52,53 The BET constant C of the hybrid material is much lower than that of the SiO2−Ex (Table 4), which indicates that the surface has become more hydrophobic. Moreover, the capillary condensation shifts to a lower range of pressures in the solid [Mn2O]@ SiO2 (Figure 5), corresponding to a pore size reduction of ∼0.7 nm. It also occurs progressively in a wider range of pressures and not in a series of steps, indicating that the Mn complex was properly spread along the whole channel. In this case, the pore size distribution is broad due to the inequality and roughness of the surface caused by the Mn complex's shape, covering values between 2.8 and 3.3 nm according to Broekhoff and de Boer (BdB) analysis.54

Characterization of the Mn(III) Complex Inside the Silica Support. The calculated formula from the elemental analysis for the [Mn2O]@SiO2 hybrid material is SiO2·0.033 [Mn2O-(2−MeOC6H4CO2)2(bpy)2]·0.005 TMA·0.35 H2O. This metal loading corresponds to ca. 66% of the cationic exchange capacity assuming two positive charges for both 1 and 2 complexes and that both X^- ions are removed. Strikingly, the remaining quantity of TMA+ ions in the solid is much less than the 34% expected for a mere cation exchange of two TMA+ per complex as it is only 5% of the initial content of SiO2−TMA. Accordingly, the missing TMA+ is removed according to another reaction that is likely neutralization. Indeed, the acetonitrile solutions of the Mn(III) compounds contain traces of water and are acidic, allowing a partial protonation of the silanolate and the release of additional TMA+ ions. The thermogravimetric analysis (TGA) shows two main mass losses in the range of 200−400 °C that are mainly assigned to the decomposition of the Mn complex's ligands and suit perfectly with the calculated formula (see more details in Supporting Information).

The IR spectrum of [Mn2O]@SiO2 contains the vibrational fingerprints of the complexes' ligands and TMA+ ions, particularly in the window of 1700−1200 cm−1 (Figure 6). Despite a weak concentration, the narrow peak at 1488 cm−1 typical of CH3 scissoring vibrational mode of the TMA+ appears in the middle of bands belonging to the ligand and attests for its presence in [Mn2O]@SiO2.40 Nearby, the bands centered at 1604, 1473, and 1442 cm−1 are assigned to the bipyridine ligand. The weak band expected at 1496 cm−1 is masked by the band assigned to TMA+ (see above). At 1558 and 1396 cm−1 arise the asymmetric and symmetric vibrations of the carboxylate groups, respectively. It is worth noting that the symmetric vibration shifts from ∼1370 (as observed in the IR spectra of compounds 1 and 2) to 1396 cm−1 when the complexes are incorporated in the silica pores, suggesting a slight change of structural parameters upon which carboxylate bridges are participating. Nevertheless, in spite of decreasing, the Δv value (Δv = va(COO) − vs(COO)) is in the range found for bidentate carboxylate ligands coordinated to two metal ions in bridging mode μ1,3.55 Moreover, the absence of bands at ∼1700 cm−1 excludes the presence of protonated carboxylate groups and consequently excludes the decoordination of these ligands. The broadening of the signals may be either due to distribution of slightly different species on the surface, caused by the heterogeneity of the environment,56 or due to dynamic effects.57

To characterize the nature of the Mn(III) complex within the silica support, X-ray absorption spectroscopy (XAS) measurements of compound 1 (as model) and material [Mn2O]@SiO2 were performed. Mn K-edge XANES and the pre-edge before the main K-edge are sensitive to the oxidation state and bonding environment of manganese.58,59 Between them, the pre-edge region is much less influenced by the medium as compared to the edge jump region.60 Compound 1 shows a pre-edge peak at 6541 eV, while for the material [Mn2O]@SiO2 two features, at 6540 and 6543 eV, could be observed (Figure S8). Moreover, for the hybrid material, the first inflection point of the Mn K-edge is shifted by 1.8 eV, in comparison to compound 1. Both factors suggest some change in the hybrid material. According to the XPS analysis and the magnetic measurements (see below), the difference between 1 and [Mn2O]@SiO2 could have been promoted by the radiation. So, this technique did not allow us to obtain valuable information about the manganese complex.

With the aim to clarify what is the oxidation state of the Mn complex inside the support, XPS measurements of compound 1 (as model) and material [Mn2O]@SiO2 were performed. The results obtained from the fit of the C 1s, the N 1s, and the Mn 3s peaks are summarized in Table S1. The C 1s signals of compound 1 and material [Mn2O]@SiO2 are very similar and are distributed in three main XPS features, assigned to Csp2 (284.6 eV), C−N and C−Oether (∼286 eV), and Ccarboxylate (∼288 eV) (Figure S9).61,62 Moreover, the C/Mn2 and N/Mn2 ratios (being 35 and 4, respectively) are consistent with the existence of the [MnIII 2O(2-MeOC6H4CO2)2(bpy)2]2+ unit in material [Mn2O]@SiO2.

Figure 7 shows the Mn 3s spectra for 1 and material [Mn2O] @SiO2. The Mn 3s doublet splitting (ΔMn 3s) provides a reliable way of determining the oxidation state of manganese, being smaller for higher oxidation state.63 Both solids display ΔMn 3s equal to 5.6 eV (Table S1), which is in agreement with those reported by J. Nelson et al. for a series of Mn(III) complexes with carboxylate and oxo bridges64 and also with the values collected in Table S2 for compounds with different oxidation states. This fact confirms that, for material [Mn2O]@ SiO2, the oxidation state of the Mn ions is III.

The N 1s spectrum of compound 1 (shown in Figure 7) displays two main peaks, assigned to the N atoms of the bpy (blue peak centered at 399.6 eV) and to the NO3 – anions (green peak centered at 406.2 eV).61 As expected, the NO3 − peak is not present in the N 1s spectrum of material [Mn2O]@ SiO2, consistent with the absence of the counteranion in the hybrid material as explained above. Indeed, the overall N/Mn2 ratio is lower for [Mn2O]@SiO2 than for 1 and agrees with two bpy ligands for each Mn2 entity, in agreement with the loss of NO3 − ions during the synthesis of the Mn−Si hybrid. Moreover, the peak around 401 eV is now split in two components, centered at 399.3 (blue) and 402.4 eV (cyan). The first and more intense peak could be assigned to Nsp2 neutral atoms,65 while the second and weaker could be attributed to some change in the coordination of one of the bpy ligands likely due to the interaction with the silica support.56,61

Magnetic measurements were also performed for material [Mn2O]@SiO2. The χMT versus T plot of this material (shown in Figure 8) indicates that there is a non-negligible interaction between the Mn ions, which strongly supports the assumption that the MnIII 2 unit is maintained in the silica pores. The χMT value at room temperature (5.8 cm3·mol−1·K) is close to the expected value for two uncoupled Mn(III) ions. The data were fitted from 300 to 17 K using the PHI program (H = −2JS1S2),46 omitting the data at low temperature (17−2 K) to avoid ZFS effects. The best fit corresponds to g = 1.98, 2J = −1.2 cm−1, Rsus = 3.4 × 10−5. The J value is between those found for 1 and 2; thus, it is also in the expected range for a [MnIII 2O(2-RC6H4COO)2]2+ subunit (between −12 and +5 cm−1).36 Unfortunately, we could not fit the whole curve due to a deviation in the low-temperature range. As it was mentioned, magnetic properties of this kind of complexes are very sensitive to structural and electronic parameters.35−37 So, this deviation may be due to the existence of more than one species that could slightly differ in some structural parameters. We achieved the fitting of the whole curve by keeping constant the parameters referred to the Mn anisotropy, with very similar values to the molecular analogues (compounds 1 and 2). However, reporting this last fit would be meaningless because it involves the assumption of unknown parameters, such as DMn, EMn, and the relative orientation of the Jahn−Teller axes of the MnIII ions.

Catalase Activity. The catalyzed disproportionation reaction of H2O2 to H2O and O2 (catalase activity) was studied with the two dinuclear MnIII compounds (1 and 2) and with material [Mn2O]@SiO2, and then the results were compared.

Catalase Activity of Compounds 1 and 2. The catalytic activity of these compounds was tested by mixing a 0.8 mM acetonitrile solution of compounds 1 or 2 and a 32% aqueous solution of H2O2, with [H2O2]0 = 1.05 M (initial concentration of H2O2) and [H2O2]0/[MnIII 2] = 1312. Note that the resulting reaction media consists of a CH3CN−H2O 9:1 (v/v) mixture. The evolution of oxygen was monitored versus time by volumetric method and then converted to turnover number (TON),

considering a two-step reaction that comprises the oxidation and reduction of H2O2. Following this definition, a TON is equal to the decomposition of two moles of H2O2 per mole of MnIII 2.

In these experiments, vigorous evolution of O2 was also observed after the addition of hydrogen peroxide. As shown in Table 5, compounds 1 and 2 are able to decompose a significant amount of H2O2 (TON ≈ 480 in 10 min), which evidences their catalytic activity. During the first minute the TON follows an almost linear tendency with time; for time >1 min, the reaction slows until reaching a plateau at ∼10 min (Figure 9). The activity of such compounds is of the same magnitude as some other analogues reported in the literature.66,67

The catalytic activity of Mn(NO3)2 and MnO2 toward H2O2 disproportionation was also investigated under the same conditions as those used for compounds 1 and 2. In both cases, the activity is ∼1 order of magnitude smaller than the one displayed by 1 and 2 during all the experiments.

According to single-crystal XRD (explained above), the crystal structures of compounds 1 and 2 is a 1:1 electrolyte, whose cation is a monocharged complex with formula [{Mn(bpy)(H2O)}(μ-2-MeOC6H4CO2)2(μ-O){Mn(bpy)- (X)}]+ with the monodentate positions occupied by water and a molecule of counteranion (X). But these last positions are quite labile, so the substitution of the X ligands is expected in solution. The molar ionic conductivity (ΛM) of an acetonitrile solution of compound 2 is 271 S·cm2·mol−1, typical for a 2:1 electrolyte solution (220−300 S·cm2·mol−1).68 This value indicates that the perchlorate anions are completely dissociated from the manganese complex. However, the ΛM of an acetonitrile solution of compound 1 (106 S·cm2·mol−1) is much lower than for 2, being close to the 1:1 electrolyte range (120−160 S cm2 mol−1).68 This is consistent with one of the nitrate ions interacting with the manganese coordination sphere. Nevertheless, the addition of a small amount of water to the solution of compound 1 (CH3CN−H2O 9:1 (v/v)) makes the ΛM increase to 189 S·cm2·mol−1, which is a higher value but still much below the characteristic range for a 2:1 electrolyte solution. These facts prove that the nitrate anion tends to interact more than the perchlorate with the Mn complex and, even though the presence of water may weaken this interaction, nitrate anions seem to remain in contact with the complex, either via hydrogen bonds or by a genuine Mn··· ONO2 interaction.

In spite of displaying very similar structures, compound 1 (X = NO3) is a better catalyst than 2 (X = ClO4); so, the cause of this difference may only lay on their X group. This fact was also reported previously by G. Fernández et al. for analogous compounds with acetate or chloroacetate bridges, where the ones with X = NO3 are also better catalysts than the ones with X = ClO4 even though they have the same cationic complex (L = H2O/H2O).69

To sum up, when 1 is in solution, nitrate ion is likely interacting with the Mn complex in acetonitrile solution, and this interaction is weakened with the presence of water. Thus, in spite of the nitrate anion being retained by the Mn complex, this could be effortlessly displaced in the presence of another group. In the case of the solid, the inner surface of material SiO2−TMA (the precursor used to form the hybrid material [Mn2O]@SiO2) is formed by silanote groups that electrostatically interact with TMA+ ions and silanol groups. The Mn complex is indeed incorporated inside the pores by ion exchange. Once the TMA+ ions are displaced by the Mn complex, the silanolate groups are free to interact with the Mn complex, this latter leaving behind the nitrate ions.

Effect of pH on the Catalase Activity of Compound 2. In the literature there are some antecedents of the pH-dependent catalase activity for different kinds of Mn complexes.70,27 Taking into account this and the possibility of the silica acting as a pH modulator, the catalase activity of 2 was evaluated at different pH values. We chose the compound with X = ClO4 (2) because this counteranion interacts less with the Mn complex in acetonitrile solution than NO3 − anion (as explained above), so its presence is likely more innocent.

Compound 2 yields a pH = 6.0 in CH3CN−H2O 9:1 (v/v). Hence, triethylamine was used to increase the basicity of the reaction media, with [Et3N]/[MnIII 2] ratios between 0 and ∼24. Figure 10 shows the

TON versus time at different pH values, and the catalytic results of this experiment are summarized in Table S3. Note that the more basic the reaction media is, the more efficient the catalyst is. Conversion close to 100% can only be reached at extremely basic pH values (pH > 12).

Catalase Activity of Material [Mn2O]@SiO2. The catalytic activity toward the H2O2 decomposition from an acetonitrile suspension of material [Mn2O]@SiO2 (0.8 mM based on [MnIII2]) was also tested under the same conditions as compounds 1 and 2 to lately be compared. It is necessary to point out that SiO2−TMA did not provoke any evolution of oxygen, which excludes any catalytic activity of the support itself for H2O2 disproportionation. Looking briefly at Figure 11, one can say that the TON versus time plot of material [Mn2O]@SiO2 has the same profile as its molecular analogues, first following a linear tendency and lately reaching a plateau. Table 6 summarizes the results obtained from the catalysis. As can be seen, the hybrid material exhibits a better catalase activity than compounds 1 and 2. The suspension of the hybrid material shows a pH = 8.9, and their activity is in the middle of those displayed for compound 2 at pH = 7.3 and 9.8. This fact suggests that one of the effects for the major activity of the material in comparison to the molecular compounds is the basic media provided by the silanolate groups of the support←the pKa of which is ∼9.71,72

A similar pH dependence was already reported in the literature for a mutated Mn catalase73 and for some MnIII2 salen complexes28,70,27 in which the catalase activity was highly improved at high pH (that guarantees the integrity of the Mn2 unit) or because of the presence of an acid−base catalytic auxiliary. In our case, the silanolate moieties in the hybrid material likely act as an endogenous acid−base auxiliary that could contribute to retain the integrity of the Mn2 core, improving its activity.

Successive additions of H2O2 were done to test if the catalyst retains its activity. As shown in Figure 12, the catalyst keeps a high activity after several additions, reaching a plateau at almost the same TON after the second and third additions (green). In spite of that, the initial rate of H2O2 dismutation for the second and third additions is lower than for the first one (red), which could be caused by the decrease observed in the pH (from 8.9 to ∼7.5).

Several EPR spectra were recorded for the solution - separating the solid - at different times, between 30 s and 2 h after the addition of H2O2. Nonsignificant EPR signal was observed in none of them, indicating that the Mn2+ content in the solution is <73 μM (limit of detection), which corresponds to 5% of the Mn in material [Mn2O]@SiO2. As the solution does not present the brown color expected for a MnIII solution, one can conclude that practically all Mn content remains inside the pores of the silica.

The isolated solid at 90 s after the addition of H2O2 was analyzed by XPS and EPR spectroscopy. The XPS displays a Mn 3s doublet splitting (ΔMn 3s) of 5.6−5.7 eV, indicating that the Mn oxidation state is mainly III (Table S2). Even though the majority of the Mn oxidation state is III, the EPR spectra (Figure S10) shows six bands in the region of g ≈ 2 with a hyperfine coupling of ∼9 mT. This pattern could be consistent with a dinuclear Mn(II) complex with a weak magnetic coupling.69 No evidence of mixed valence systems (MnII−MnIII or MnIII−MnIV) was observed. These facts suggest that catalytic species involves MnII and MnIII oxidation states and that it mainly remains inside the pores. However, the XPS analysis of this sample shows a lower N/Mn2 ratio than that of the former material [Mn2O]@SiO2. This could be indicative of a partial unfastening of the bpy ligand from the solid. As it was indicated, in the hybrid material some N atoms of the bpy ligand could interact with the silanolate groups of the wall, suggesting a quite weak Mn−N bond. During the catalytic process, the strength of this bond could decrease, the bpy ligand being more labile. Therefore, the partial release of the bpy from the hybrid material could probably be due to the treatment of the sample (washing and drying) before the measurements.

Catalase Activity in Aqueous Media of 1, 2, and [Mn2O]@ SiO2. In contrast to the activity in acetonitrile (see above), compounds 1 and 2 are not good catalysts in water solution, hardly

decomposing ~5% of the [H2O2]0 in 10 min (Table 7). This is predictable since Mn2 compounds have low stability in aqueous media.22

However, the hybrid material shows catalase activity in aqueous media. As showed in Figure 13 and Table 7, material [Mn2O]@SiO2 is able to reach TON ≈ 400 in 5 min with linear tendency. Then, it approaches an asymptotic value of 514 at 10 min. Nevertheless, the activity of this material in water is lower than in acetonitrile, especially in the first minute.

Stability of Material [Mn2O]@SiO2. The morphology and characteristics of material [Mn2O]@SiO2 after the 2 h reactions with H2O2 in CH3CN−H2O 9:1 (v/v) ([Mn2O]@SiO2 #A) and in water ([Mn2O]@SiO2 #W) were analyzed. The results are summarized in Table 8.

Material [Mn2O]@SiO2 #A preserves the mesostructure and porosity of the former material [Mn2O]@SiO2, as observed in the XRD pattern and the N2 sorption isotherms (Figure S11). Nevertheless, the pore volume is higher than the one observed for [Mn2O]@SiO2, and the mass loss corresponding to the Mn complex's ligands decreased, suggesting that the pores are less loaded. This fact is in agreement with the XPS analysis performed on the isolated solid during the reaction (explained above).

Contrary to the previous one, material [Mn2O]@SiO2 #W displayed a poor XRD pattern and N2 sorption isotherms without a clear capillary condensation (Figure S12), meaning that the mesostructure was disrupted after the reaction with H2O2.

To know whether this fact is due to the water or the H2O2, the stability of material [Mn2O]@SiO2 was also checked in water suspension. After 2 h of treatment, the resulting solid ([Mn2O]@SiO2 #M) displays the typical N2 sorption isotherms of a mesostructured material (Figure S13). So, the support itself is not disrupted by the presence of water; but it has also a higher pore volume than its former material ([Mn2O]@SiO2).

To summarize, the presence of water is not responsible for the damage of the mesostructure of the support; this is only altered when both water and H2O2 are present. In addition, the water and the reaction with H2O2 favor the release of part of the bpy ligands. However, the loss of loading could occur during the process of isolation of the solid.

These facts could be attributed to the nudity of the silica's inner surface. Even though the ultrafast microwave-assisted synthesis leads to highly ordered and chemically stable mesoporous silica,41 the pore surface is formed by Q3 (mainly) and Q2 silanol groups, which are sensitive to nucleophilic attacks and to strong oxidants. Therefore, modification of the silica's internal surface is under progress to overcome these limitations. Hydrophobization and covering of the pore surface would hopefully limit the internal water diffusion and increase the stability of both the Mn complex and the structure of the nanochannels.

CONCLUSIONS

Two dinuclear manganese(III) compounds with formula [{Mn(bpy)(H2O)}(μ-2-MeOC6H4CO2)2(μ-O){Mn(bpy)- (X)}]X (X = NO3 or ClO4) have been synthesized (only differing in the counteranion) and structurally and magnetically characterized. The crystal structure reveals that the anions tend to be coordinated to one manganese ion, occupying one monodentate position. The distortion of the coordination octahedron of the manganese ion depends on this monodentate ligand, being more elongated with X = ClO4. The antiferromagnetic interaction between the Mn(III) ions is affected by the structural parameters, mostly by the relative disposition of the Jahn−Teller axes. The almost orthogonal disposition of these axes together with a negative value of the ZFS parameter (DMn) are relevant on the magnetic behavior at low temperature. These compounds are structural and functional models of the Mn-catalase, being able to catalyse the H2O2 decomposition in CH3CN−H2O 9:1 (v/v) solution. Compound 1, with nitrate as counteranion and labile ligand, is more efficient than compound 2 (X = ClO4).

The insertion of compounds 1 and 2 into mesoporous silica, by ionic exchange, leads to the same material, indicating that only the cationic complex is grafted inside the support. The analysis of the new material shows that the Mn complex occupies half of the available mesoporous volume within the pores and that the hexagonal array was unaltered upon the insertion of the Mn complex. Moreover, a non-negligible antiferromagnetic interaction between Mn(III) ions was observed, indicating that the dinuclear unit is preserved inside the silica.

The hybrid material shows also catalase activity, and it is more efficient than the coordination compounds 1 and 2. This fact is due to the presence of silanolate groups that likely buffers a basic pH and favors the catalyzed H2O2 decomposition. According to EPR spectroscopy and XPS analysis, the reaction seems to take place inside the support and that the Mn oxidation state swings between II and III. The insertion of the coordination compound inside the mesoporous silica provides a good way to protect the catalytic center from the external media and opens a new approach to work with manganese compounds in aqueous media, paving the way toward the application of these active antioxidant species at physiological conditions.

AUTHOR INFORMATION

Corresponding Authors

*E-mail: luis.escrichetur@gmail.com.

*E-mail: belen.albela@ens-lyon.fr.

Notes

The authors declare no competing financial interest

ACKNOWLEDGEMENTS

This work was supported by the Ministerio de Ciencia e Innovación of Spain (Project Nos. CTQ2012-30662 and CTQ2010-15364), the Agència de Gestió d'Ajuts Universitaris i de Recerca (AGAUR) of la Generalitat de Catalunya (Project No. 2009-SGR1454), the Region Rhône-Alpes of France (Project No. COOPERA-C-1349S81), the Generalitat Valenciana (Project No. ISIC2012/002), and the Consorcio para la Construcción, Equipamiento y Explotación del Laboratorio de Luz Sincrotrón (CELLS; Project No. 2012100444-3). L.E. thanks the Univ. of Barcelona for the APIF fellowship and the C-MIRA program of the Region Rhône-Alpes in France for the financial support to the collaboration between the Univ. of Barcelona (Spain) and the École Normale Supérieure de Lyon (France). XAS experiments were performed at BL22 (CLÆSS) beamline at ALBA Synchrotron Light Facility with the collaboration of ALBA staff. In particular, we thank C. Marini for his help in the normalization of spectra. We are also very thankful to F. Vadcard, S. Speed, and N. Calin for their contribution to TEM, the resolution of crystal structures, and powder XRD measurements, respectively. Finally, we show L. Calvo and N. Iranzo gratitude for their help with the treatment and interpretation of the XPS data.

REFERENCES

(1) Lippard, S. J.; Berg, J. M. Principles of Bioinorganic Chemistry; University Science Books, 1994.

(2) Imlay, J. A. Nat. Rev. Microbiol. 2013, 11, 443−454.

(3) Nathan, C.; Cunningham-Bussel, A. Nat. Rev. Immunol. 2013, 13, 349−361.

(4) Walling, C. Acc. Chem. Res. 1975, 8, 125−131.

(5) Costa, V.; Moradas-Ferreira, P. Mol. Aspects Med. 2001, 22, 217−246.

(6) Sayre, L. M.; Perry, G.; Smith, M. A. Chem. Res. Toxicol. 2008, 21, 172−188.

(7) Warner, D. S.; Sheng, H.; Batinić-Haberle, I. J. Exp. Biol. 2004, 207, 3221−3231.

(8) Valko, M.; Leibfritz, D.; Moncol, J.; Cronin, M. T. D.; Mazur, M.; Telser, J. Int. J. Biochem. Cell Biol. 2007, 39, 44−84.

(9) Watson, J. Open Biol. 2013, 3, 120144.

(10) Day, B. J. Biochem. Pharmacol. 2009, 77, 285−296.

(11) Day, B. J. Drug Discovery Today 2004, 9, 557−566.

(12) Batinić-Haberle, I.; Rebouças, J. S.; Spasojević, I. Antioxid. Redox Signaling 2010, 13, 877−918.

(13) Day, B. J. Antioxid. Redox Signaling 2007, 10, 355−370.

(14) Escribano, A.; Amor, M.; Pastor, S.; Castillo, S.; Sanz, F.; Codoñer-Franch, P.; Dasí, F. Thorax 2015, 70, 82−83.

(15) Offen, D.; Melamed, E.; Gilgun-Sherki, Y. J. Neurol. 2004, 251, 261−268.

(16) Karlík, M.; Valkovič, P.; Hančinová, V.; Krížová, L.; Tóthová, L.; Celec, P. Clin. Biochem. 2015, 48, 24−28.

(17) Geldenhuys, W. J.; Darvesh, A. S. Expert Rev. Neurother. 2015, 15, 3−5.

(18) Colamartino, M.; Santoro, M.; Duranti, G.; Sabatini, S.; Ceci, R.; Testa, A.; Padua, L.; Cozzi, R. Neurotoxic. Res. 2015, 27, 106−117.

(19) Jaffer, O. A.; Carter, A. B.; Sanders, P. N.; Dibbern, M. E.; Winters, C. J.; Murthy, S.; Ryan, A. J.; Rokita, A. G.; Prasad, A. M.; Zabner, J.; Kline, J. N.; Grumbach, I. M.; Anderson, M. E. Am. J. Respir. Cell Mol. Biol. 2015, 52, 106−115.

(20) Tataranno, M. L.; Perrone, S.; Longini, M.; Buonocore, G. Oxid. Med. Cell. Longevity 2015, 2015, No. 108251, DOI: 10.1155/2015/108251.

(21) Whittaker, J. W. Arch. Biochem. Biophys. 2012, 525, 111−120.

(22) Signorella, S.; Hureau, C. Coord. Chem. Rev. 2012, 256, 1229−1245.

(23) Kubota, R.; Asayama, S.; Kawakami, H. Chem. Commun. 2014, 50, 15909−15912.

(24) Ledesma, G. N.; Eury, H.; Anxolabéhère-Mallart, E.; Hureau, C.; Signorella, S. R. J. Inorg. Biochem. 2015, 146, 69−76.

(25) Kar, P.; Drew, M. G. B.; Ghosh, A. Inorg. Chim. Acta 2013, 405, 349−355.

(26) Kubota, R.; Imamura, S.; Shimizu, T.; Asayama, S.; Kawakami, H. ACS Med. Chem. Lett. 2014, 5, 639−643.
(27) Noritake, Y.; Umezawa, N.; Kato, N.; Higuchi, T. Inorg. Chem. 2013, 52, 3653−3662.
(28) Palopoli, C.; Duhayon, C.; Tuchagues, J.-P.; Signorella, S. Dalton Trans 2014, 43, 17145−17155.
(29) Reinert, P.; Garcia, B.; Morin, C.; Badiei, A.; Perriat, P.; Tillement, O.; Bonneviot, L. Stud. Surf. Sci. Catal. 2003, 146, 133−136.
(30) Beck, J. S.; Vartuli, J. C.; Roth, W. J.; Leonowicz, M. E.; Kresge, C. T.; Schmitt, K. D.; Chu, C. T. W.; Olson, D. H.; Sheppard, E. W. J. Am. Chem. Soc. 1992, 114, 10834−10843.
(31) Zhang, K.; Chen, H.-L.; Albela, B.; Jiang, J.-G.; Wang, Y.-M.; He, M.-Y.; Bonneviot, L. Eur. J. Inorg. Chem. 2011, 2011, 59−67.
(32) Chaignon, J.; Stiriba, S.-E.; Lloret, F.; Yuste, C.; Pilet, G.; Bonneviot, L.; Albela, B.; Castro, I. Dalton Trans. 2014, 43, 9704−9713.
(33) Du, L.; Li, J.; Chen, C.; Liu, Y. Free Radical Res. 2014, 48, 1061−1069.
(34) Vivero-Escoto, J. L.; Slowing, I. I.; Trewyn, B. G.; Lin, V. S.-Y. Small 2010, 6, 1952−1967.
(35) Fernández, G.; Corbella, M.; Aullón, G.; Maestro, M. A.; Mahía, J. Eur. J. Inorg. Chem. 2007, 2007, 1285−1296.
(36) Gómez, V.; Corbella, M.; Roubeau, O.; Teat, S. J. Dalton Trans. 2011, 40, 11968.
(37) Gómez, V.; Corbella, M.; Aullón, G. Inorg. Chem. 2010, 49, 1471−1480.
(38) Sala, T.; Sargent, M. V. J. Chem. Soc., Chem. Commun. 1978, 6, 253−254.
(39) Bonneviot, L.; Morin, M.; Badiel, A. Patent WO 01/55031 A1, 2001.
(40) Zhang, K.; Albela, B.; He, M.-Y.; Wang, Y.; Bonneviot, L. Phys. Chem. Chem. Phys. 2009, 11, 2912.
(41) Chaignon, J.; Bouizi, Y.; Davin, L.; Calin, N.; Albela, B.; Bonneviot, L. Green Chem. 2015, 17, 3130−3140.
(42) SADABS, Version 2008/1; Sheldrick, Bruker AXS Inc., 2008.
(43) Sheldrick, G. M. Acta Crystallogr., Sect. A: Found. Crystallogr. 2008, 64, 112−122.
(44) Gagliardi, L. G.; Castells, C. B.; Ràfols, C.; Rosés, M.; Bosch, E. Anal. Chem. 2007, 79, 3180−3187.
(45) Kahn, O. Molecular Magnetism; VCH, 1993.
(46) Chilton, N. F.; Anderson, R. P.; Turner, L. D.; Soncini, A.; Murray, K. S. J. Comput. Chem. 2013, 34, 1164−1175.
(47) Aromí, G.; Telser, J.; Ozarowski, A.; Brunel, L.-C.; Stoeckli-Evans, H.-M.; Krzystek, J. Inorg. Chem. 2005, 44, 187−196.
(48) Duboc, C.; Ganyushin, D.; Sivalingam, K.; Collomb, M.-N.; Neese, F. J. Phys. Chem. A 2010, 114, 10750−10758.
(49) Boča, R. Coord. Chem. Rev. 2004, 248, 757−815.

(50) Gomez-Coca, S.; Cremades, E.; Aliaga-Alcalde, N.; Ruiz, E. J. Am. Chem. Soc. 2013, 135, 7010−7018.
(51) Sing, K. S. W. Pure Appl. Chem. 1985, 57, 603−619.
(52) Abry, S.; Lux, F.; Albela, B.; Artigas-Miquel, A.; Nicolas, S.; Jarry, B.; Perriat, P.; Lemercier, G.; Bonneviot, L. Chem. Mater. 2009, 21, 2349−2359.
(53) Calmettes, S.; Albela, B.; Hamelin, O.; Ménage, S.; Miomandre, F.; Bonneviot, L. New J. Chem. 2008, 32, 727.
(54) Broekhoff, J. C. P.; De Boer, J. H. J. Catal. 1967, 9, 15−27.
(55) Deacon, G. B.; Phillips, R. J. Coord. Chem. Rev. 1980, 33, 227−250.
(56) Abry, S.; Thibon, A.; Albela, B.; Delichère, P.; Banse, F.; Bonneviot, L. New J. Chem. 2009, 33, 484.
(57) Zhang, K.; Lam, K.-F.; Albela, B.; Xue, T.; Khrouz, L.; Hou, Q.-W.; Yuan, E.-H.; He, M.-Y.; Bonneviot, L. Chem. - Eur. J. 2011, 17, 14258−14266.
(58) Manceau, A.; Marcus, M. A.; Grangeon, S. Am. Mineral. 2012, 97, 816−827.
(59) Bossek, U.; Hummel, H.; Weyhermüller, T.; Wieghardt, K.; Russell, S.; van der Wolf, L.; Kolb, U. Angew. Chem., Int. Ed. Engl. 1996, 35, 1552−1554.
(60) Chalmin, E.; Farges, F.; Brown, G. E., Jr Contrib. Mineral. Petrol. 2009, 157, 111−126.
(61) Moulder, J. F. Handbook of X-ray Photoelectron Spectroscopy: A Reference Book of Standard Spectra for Identification and Interpretation of XPS Data; Physical Electronics Division, Perkin-Elmer Corporation, 1992.
(62) Bratt, A.; Barron, A. R. XPS of Carbon Nanomaterials; Openstax CNX, 2011.
(63) Cerrato, J. M.; Hochella, M. F.; Knocke, W. R.; Dietrich, A. M.; Cromer, T. F. Environ. Sci. Technol. 2010, 44, 5881−5886.
(64) Nelson, A. J.; Reynolds, J. G.; Christou, G. J. Appl. Phys. 2003, 93, 2536−2539.
(65) García-Martín, J.; López-Garzón, R.; Godino-Salido, M. L.; Cuesta-Martos, R.; Gutiérrez-Valero, M. D.; Arranz-Mascarós, P.; Stoeckli-Evans, H. Eur. J. Inorg. Chem. 2005, 2005, 3093−3103.
(66) Corbella, M.; Fernández, G.; González, P.; Maestro, M.; Font-Bardia, M.; Stoeckli-Evans, H. Eur. J. Inorg. Chem. 2012, 2012, 2203−2212.
(67) Gómez, V.; Corbella, M. Eur. J. Inorg. Chem. 2012, 2012, 3147−3155.
(68) Geary, W. J. Coord. Chem. Rev. 1971, 7, 81−122.
(69) Fernández, G.; Corbella, M.; Alfonso, M.; Stoeckli-Evans, H.; Castro, I. Inorg. Chem. 2004, 43, 6684−6698.
(70) Palopoli, C.; Bruzzo, N.; Hureau, C.; Ladeira, S.; Murgida, D.; Signorella, S. Inorg. Chem. 2011, 50, 8973−8983.
(71) Iler, R. K. The Chemistry of Silica: Solubility, Polymerization, Colloid and Surface Properties and Biochemistry of Silica; Wiley-Interscience: New York, 1979.

(72) Calmettes, S. Conception d'un catalyseur par greffage d'un complexe de rutheń ium en milieu confiné ; Application à l'oxydation seĺ ective. Ph.D. Thesis, Ecole Normale Supeŕ ieure de Lyon-ENS LYON; Université Claude Bernard-Lyon I: France, 2008.

(73) Whittaker, M. M.; Barynin, V. V.; Igarashi, T.; Whittaker, J. W. Eur. J. Biochem. 2003, 270, 1102−1116. Inorganic Chemistry Article DOI

.

836 **Legends to figures**

837

838 **Figure 1** Crystal structure of the cationic complex of compound 1. Hydrogen atoms were omitted for
839 clarity.

840

841 **Figure 2.** Crystal structure of the cationic complex of compound 2.Hydrogen atoms were omitted for
842 clarity.

843

844 **Figure 3** Figure 3. χMT vs T plots for compounds 1 (blue) and 2 (green); and M/Nμβ vs HT plot (inset)
845 for compound 2 at six different values of the magnetic field. The solid lines are the best fits of the
846 experimental data.

847

848 **Fig. 4** Figure 4. Synthetic procedure to obtain the Mn−SiO2-based material [Mn2O]@SiO2 from "as-
849 made" silica (SiO2−CTA). The insertion performed from compound 1 or 2 leads to the same material.
850 Abbreviations: CTA+, cetyltrimethylammonium; TMA+, tetramethylammonium.

851

852 **Figure 5.** N2 adsorption (●) and desorption (○) isotherms at 77 K of materials SiO2−Ex (blue),
853 SiO2−TMA (green), and [Mn2O]@SiO2 (red).

854

855 **Figure 6.** Infrared spectra (range 1800−1100 cm−1) of compound 1 (blue), compound 2 (green) and
856 material [Mn2O]@SiO2 (red). The star (*), the arrows (↓), and circles (●) indicate IR vibrations of
857 TMA+, carboxylate, and bipyridine, respectively.

858

859 **Figure 7**. XPS spectra of Mn 3s (a, b) and N 1s (c, d) peaks for compound 1 (a, c) and material
860 [Mn2O]@SiO2 (b, d). The solid black lines correspond to the experimental plots; the dotted lines
861 correspond to the background, and the colored lines to the deconvoluted curves.

862

863 **Figure 8**. χMT vs T plots for compounds 1 (blue), 2 (green), and material [Mn2O]@SiO2 (red). The
864 solid lines are the best fits of the experimental data.

865

866 **Figure 9.** Catalase activity of a 0.8 mM solutions of compounds 1 (blue) and 2 (green) in
867 acetonitrile−water 9:1 (v/v), with [H2O2]0 = 1.05 M.

868

869 **Figure 10.** Catalase activity of 0.8 mM solutions of compound 2 in acetonitrile−water 9:1 (v/v) at
870 different pH values, with [H2O2]0 = 1.05 M.

871

Figure 11. Catalase activity of material [Mn2O]@SiO2 (0.8 mM based on [MnIII2]) (red) and for compound 2 at pH = 7.3 (green) and 9.8 (orange) in acetonitrile−water 9:1 (v/v), with [H2O2]0 = 1.05 M.

Figure 12. Turnover number vs time for three successive additions (at t = 0, 500, and 1230 s) of H2O2 (1312 equiv) to a suspension of material [Mn2O]@SiO2 (0.8 mM based on [MnIII2]) in CH3CN−H2O 9:1 (v/v). Red lines correspond to the initial rate of H2O2 dismutation, and the green lines correspond to the saturation TON after each addition.

Figure 13. Turnover number vs time for 1 (blue), 2 (green), and [Mn2O]@SiO2 (0.8 mM based on [MnIII2]) (red) in water, with [H2O2]0 = 1.05 M.

FIGURE 1

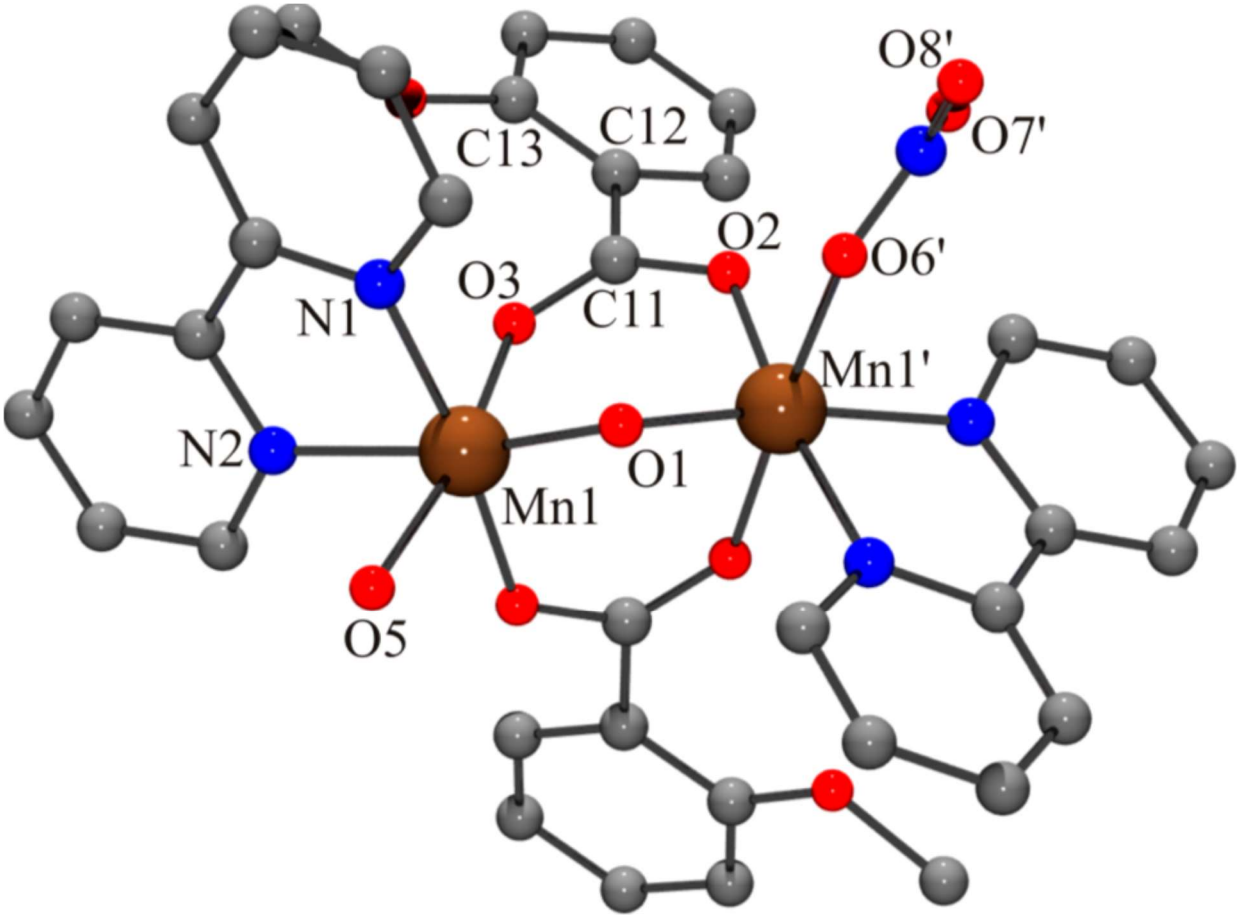

FIGURE 2

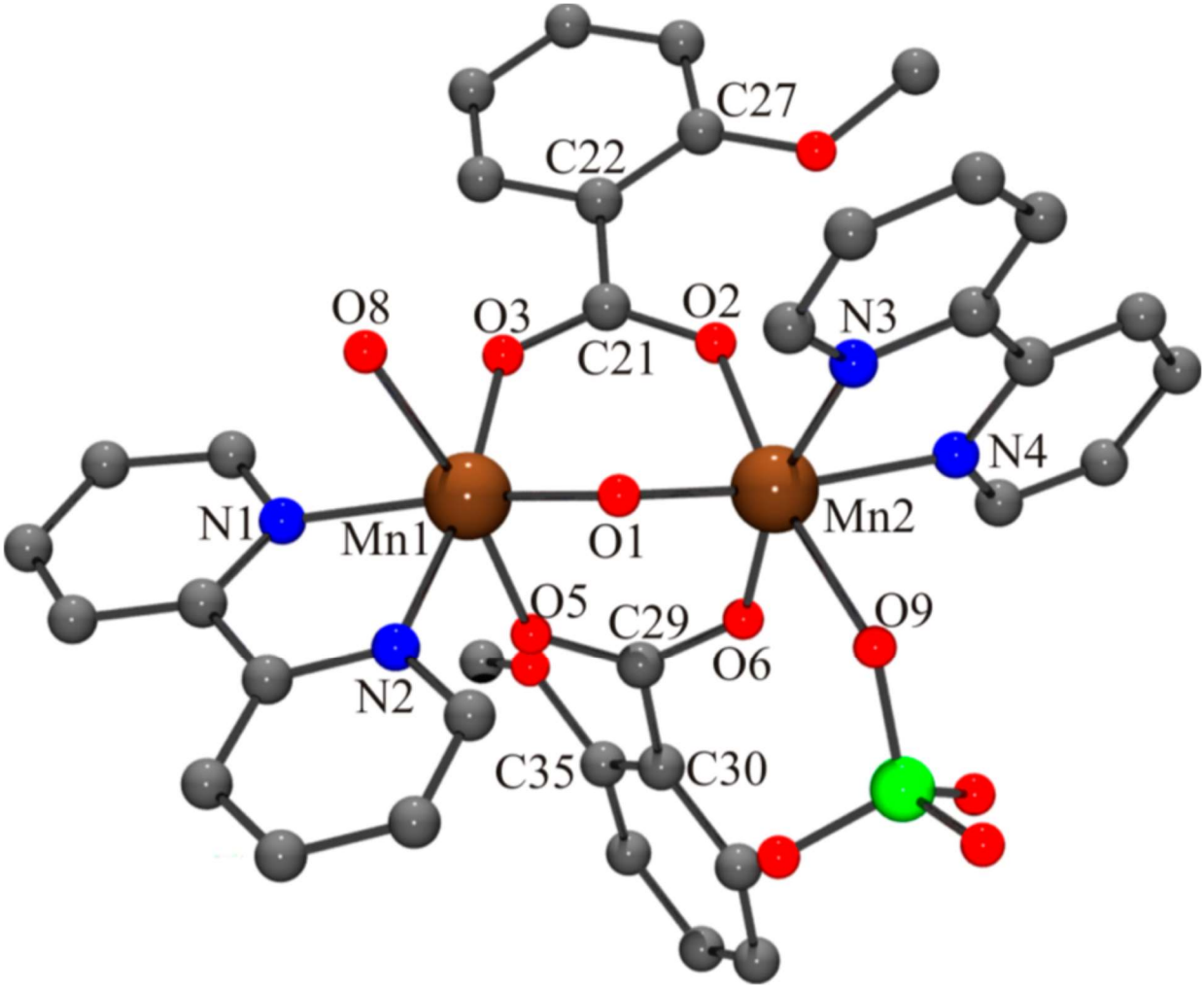

FIGURE 3

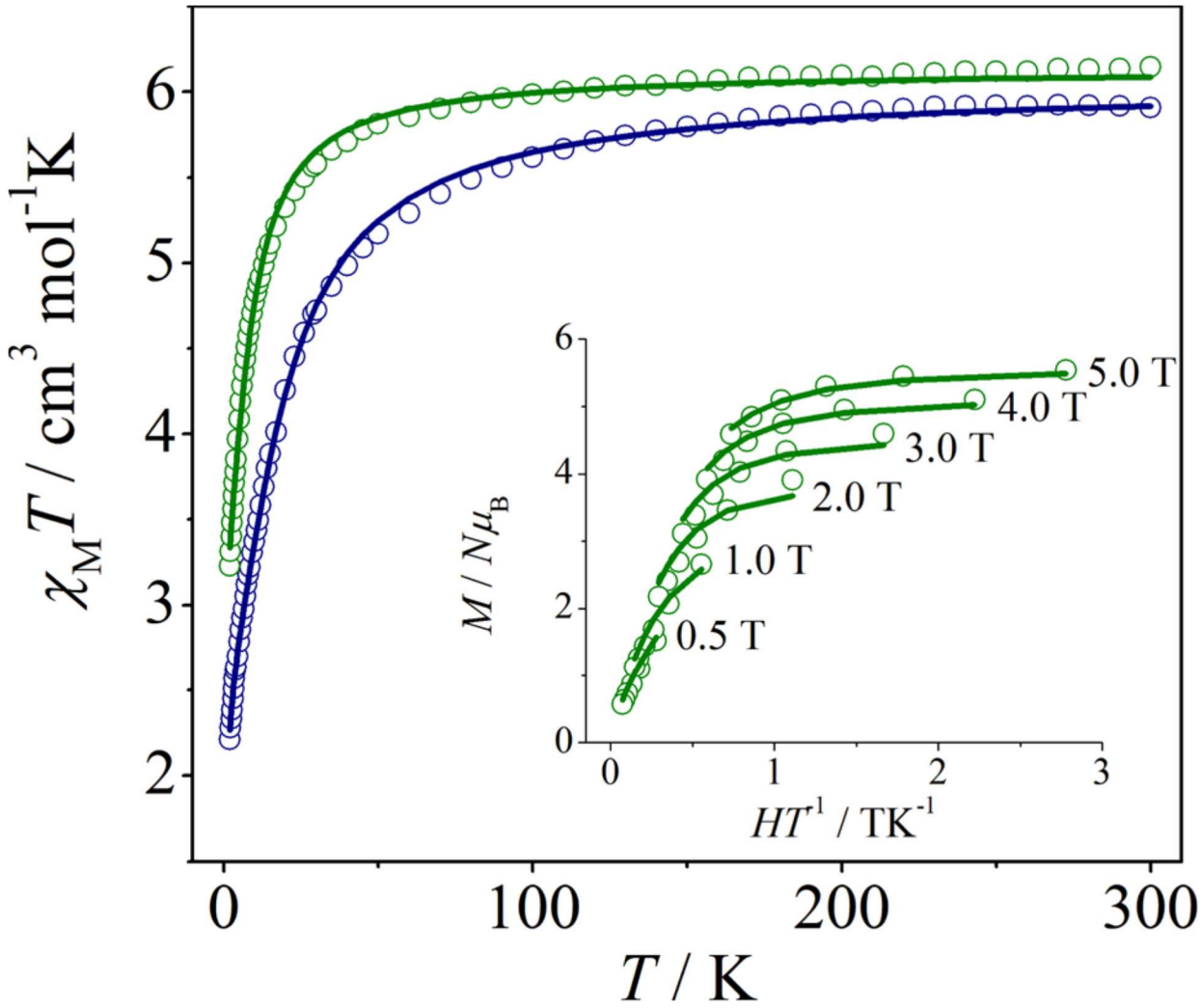
$\chi_M T$ / cm^3 mol^{-1}K
T / K
0
100
200
300
2
3
4
5
6
M / $N\mu_B$
HT^{-1} / TK^{-1}
0
1
2
3
5.0 T
4.0 T
3.0 T
2.0 T
1.0 T
0.5 T

907 **FIGURE 4**

908

909

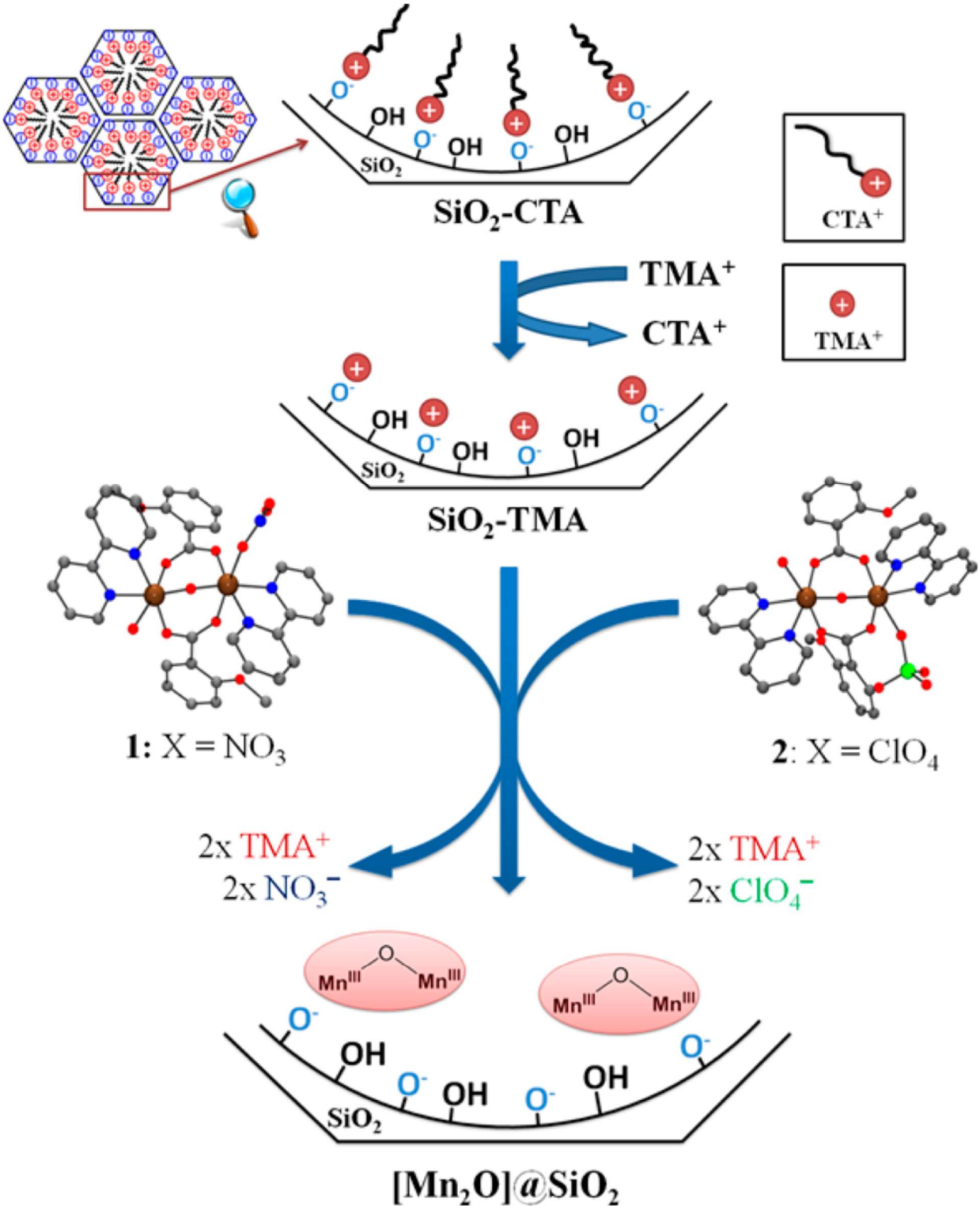

910

911

FIGURE 5

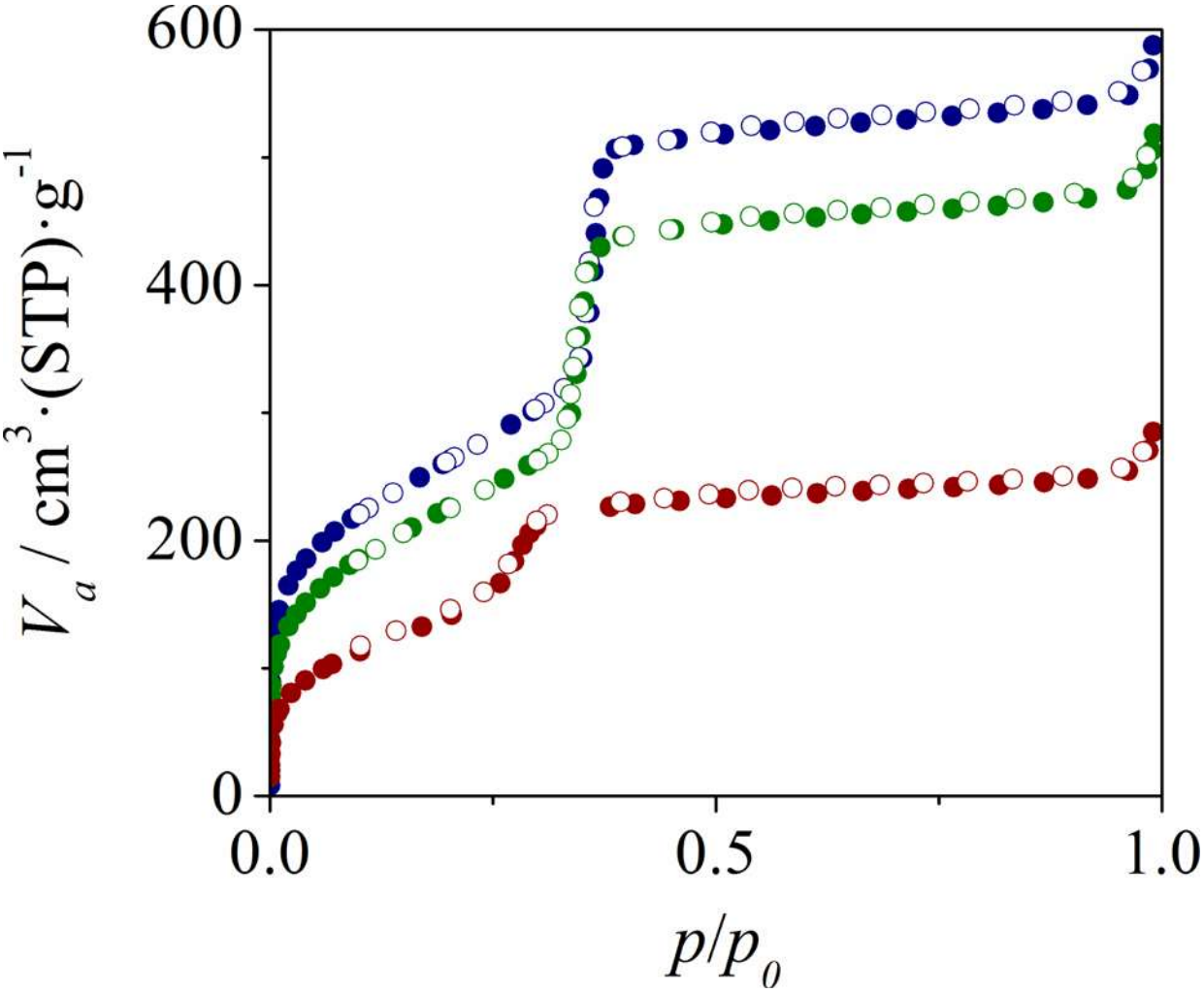

FIGURE 6

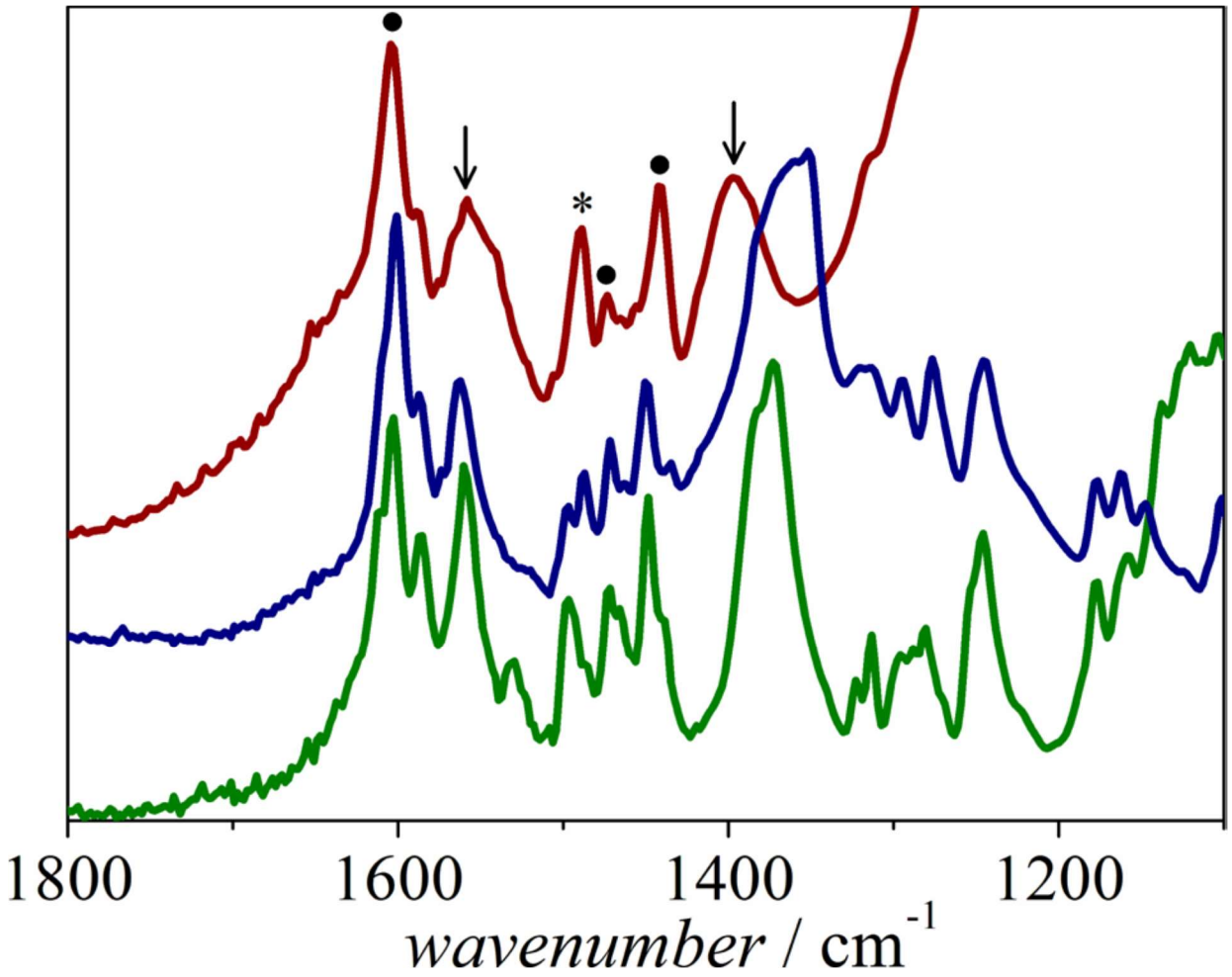

929
930
931

FIGURE 7

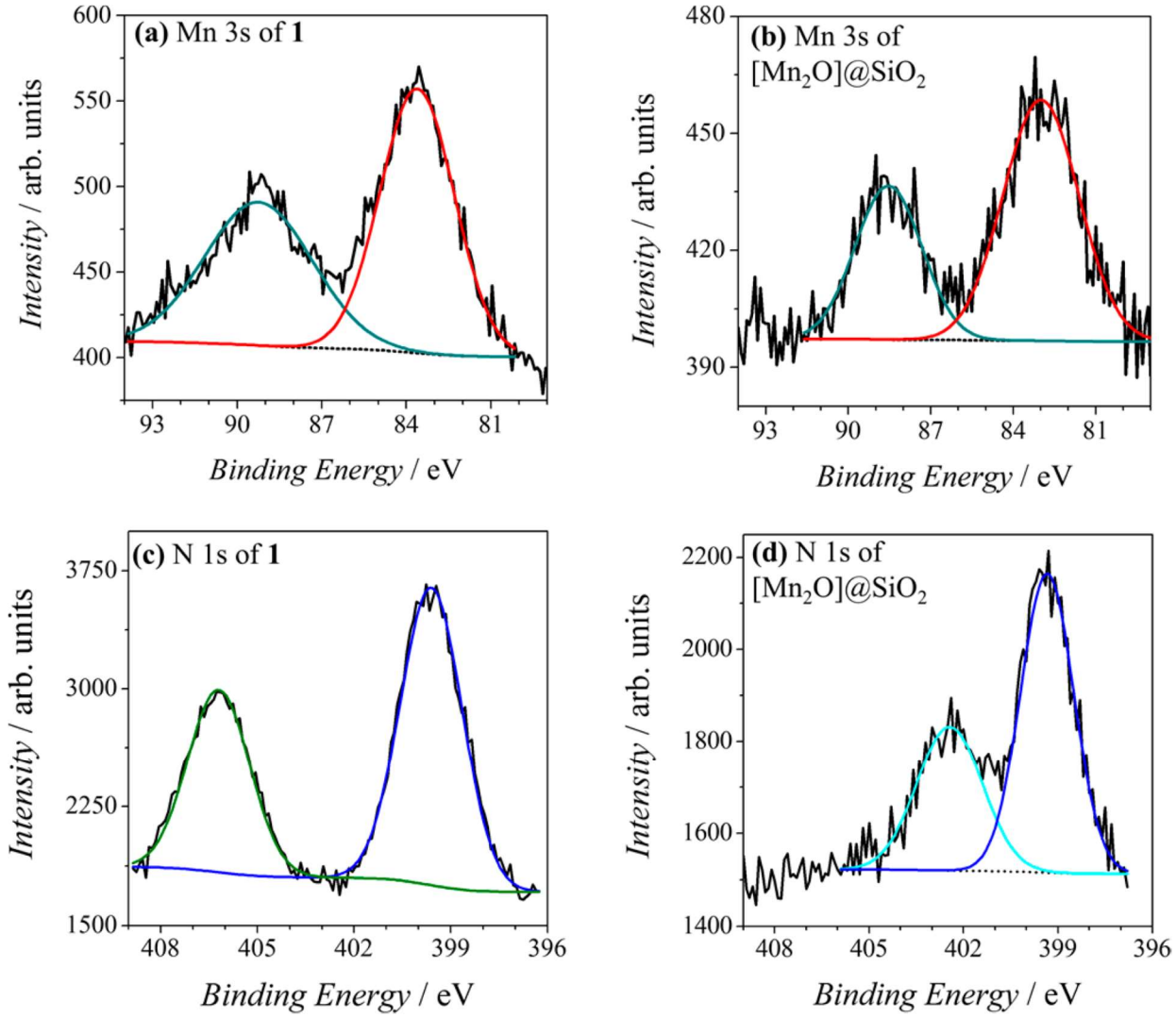

932
933

934
935
936

FIGURE 8

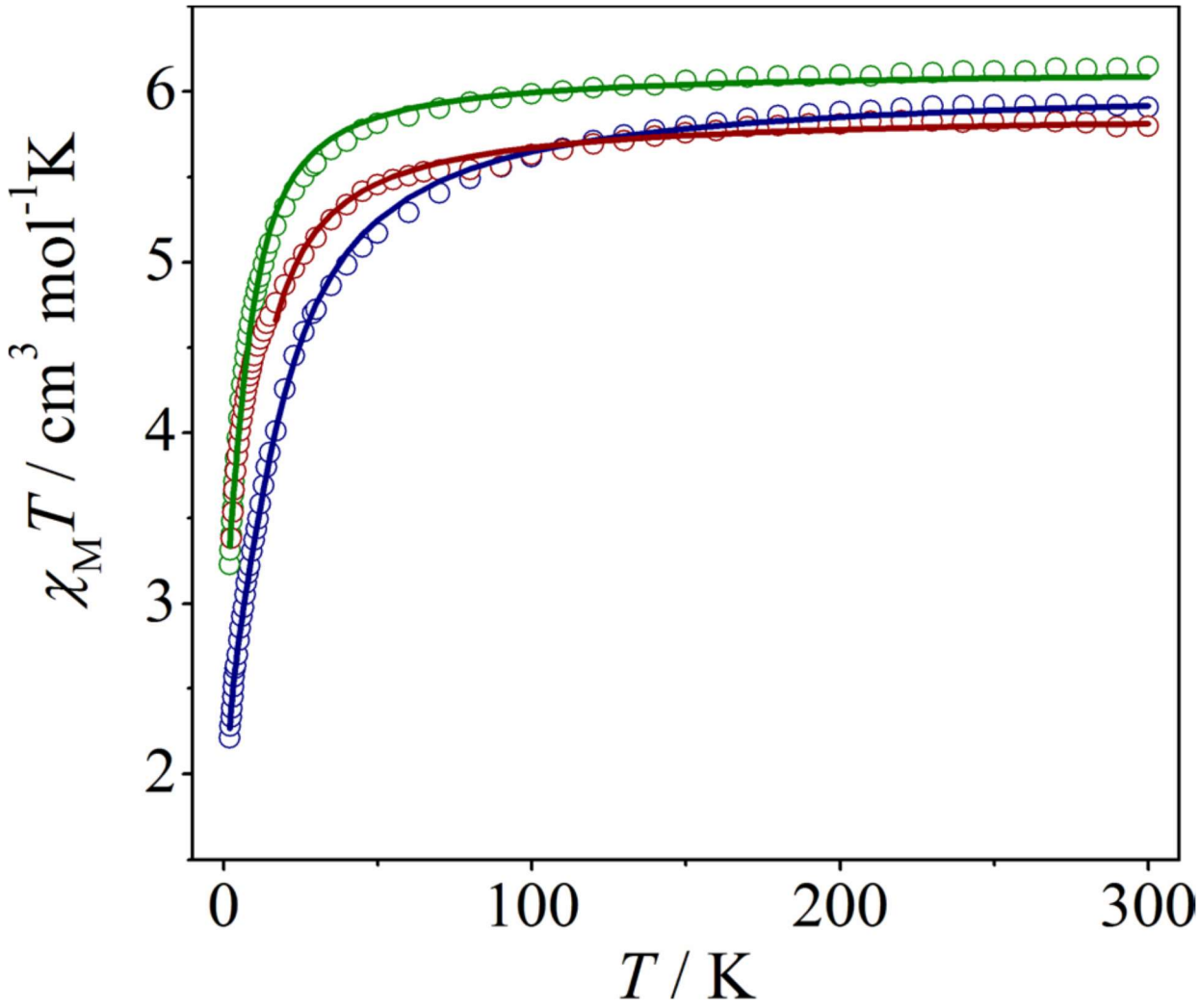

937
938

FIGURE 9

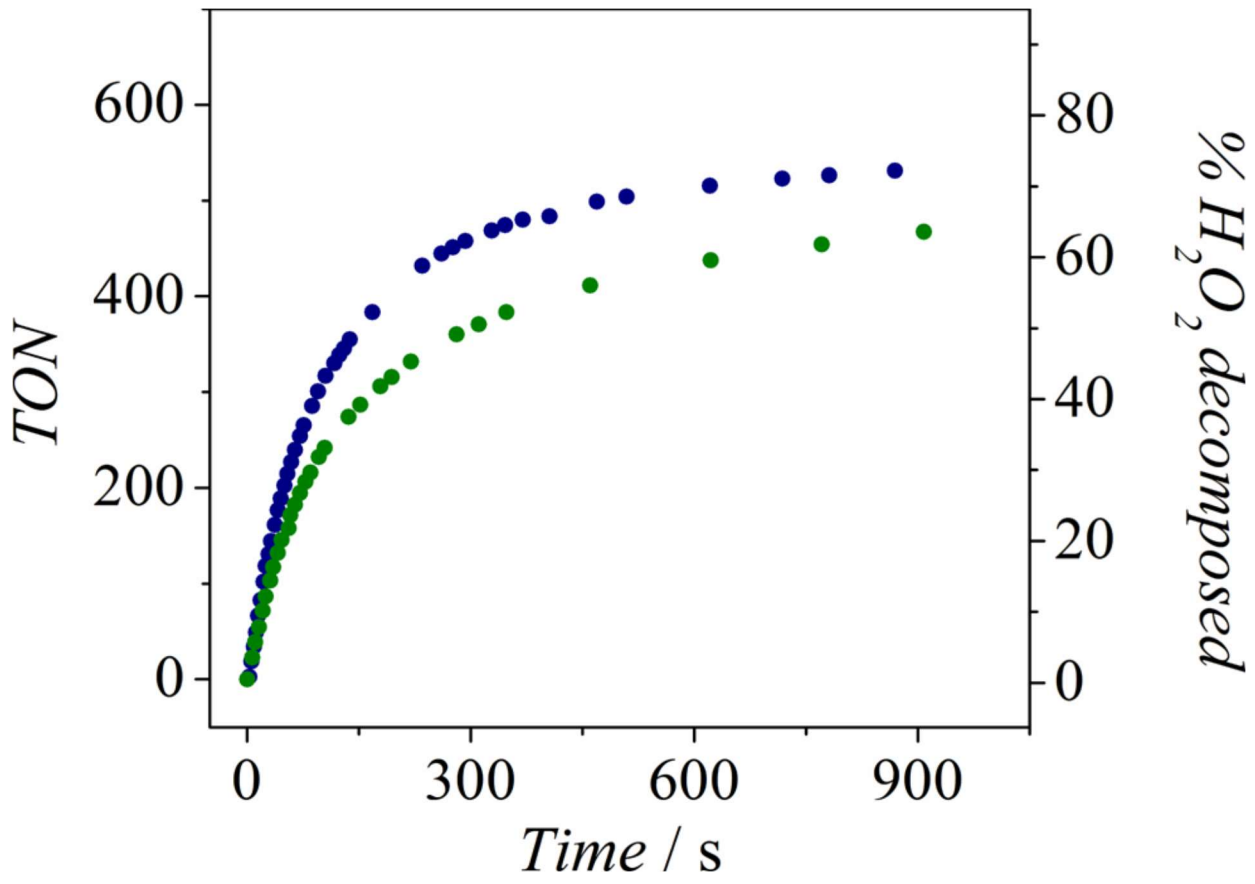
600
400
200
0
TON
80
60
40
20
0
% H2O2 decomposed
0
300
600
900
Time / s

FIGURE 10

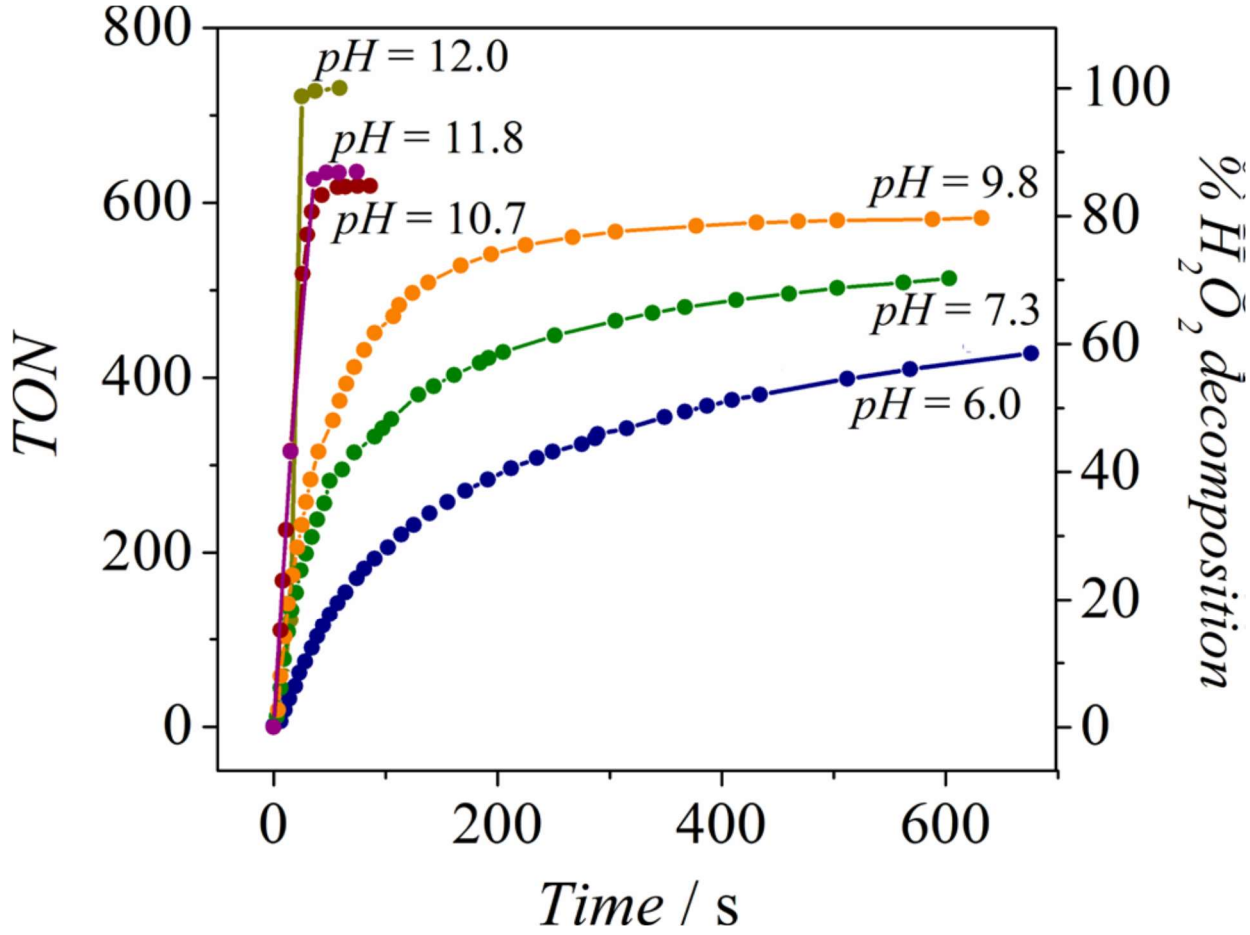
pH = 12.0
pH = 11.8
pH = 10.7
pH = 9.8
pH = 7.3
pH = 6.0
TON
% H2O2 decomposition
Time / s
0
200
400
600
800
0
20
40
60
80
100

FIGURE 11

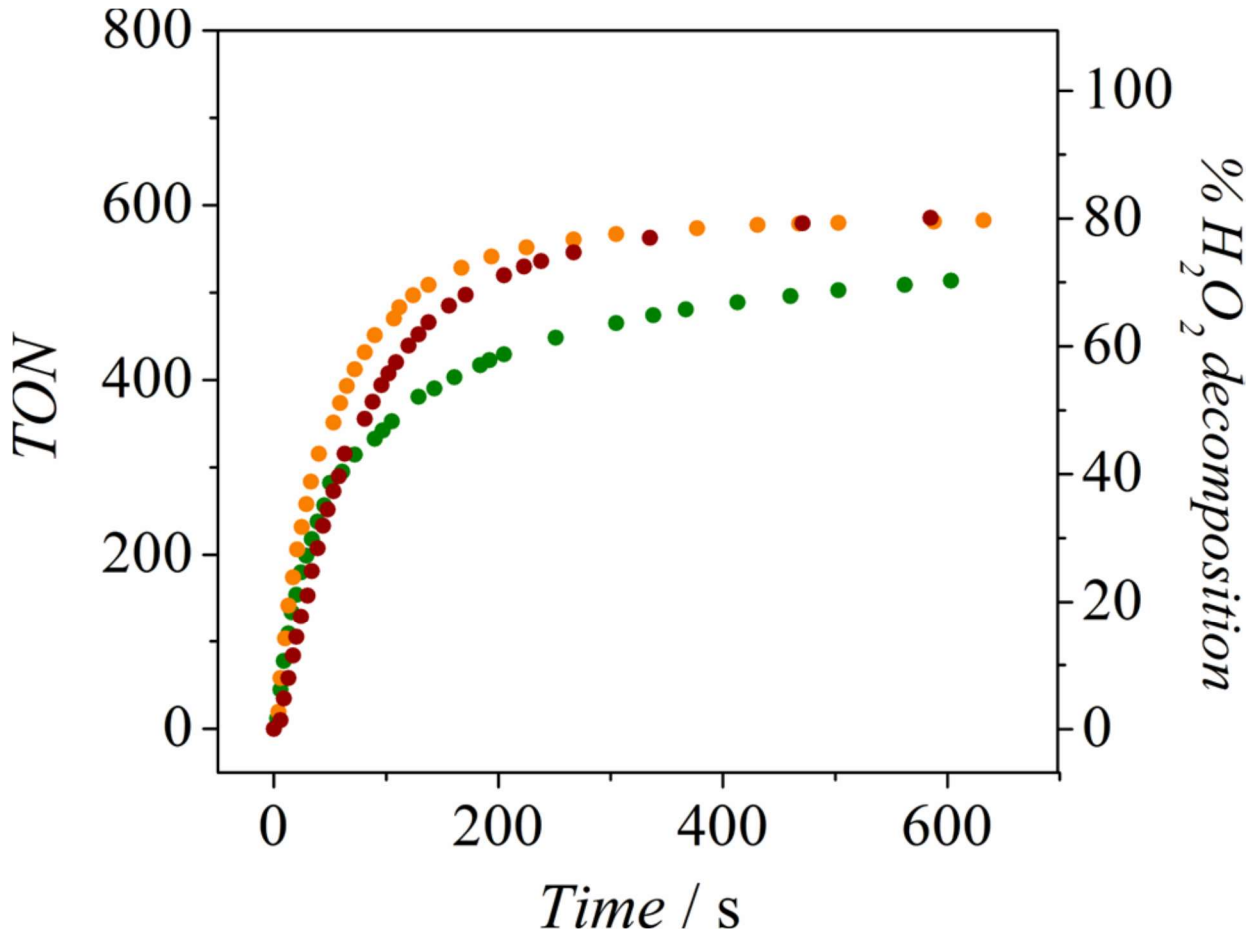
800
600
400
200
0
TON
100
80
60
40
20
0
% H2O2 decomposition
0
200
400
600
Time / s

959
960
961

FIGURE 12

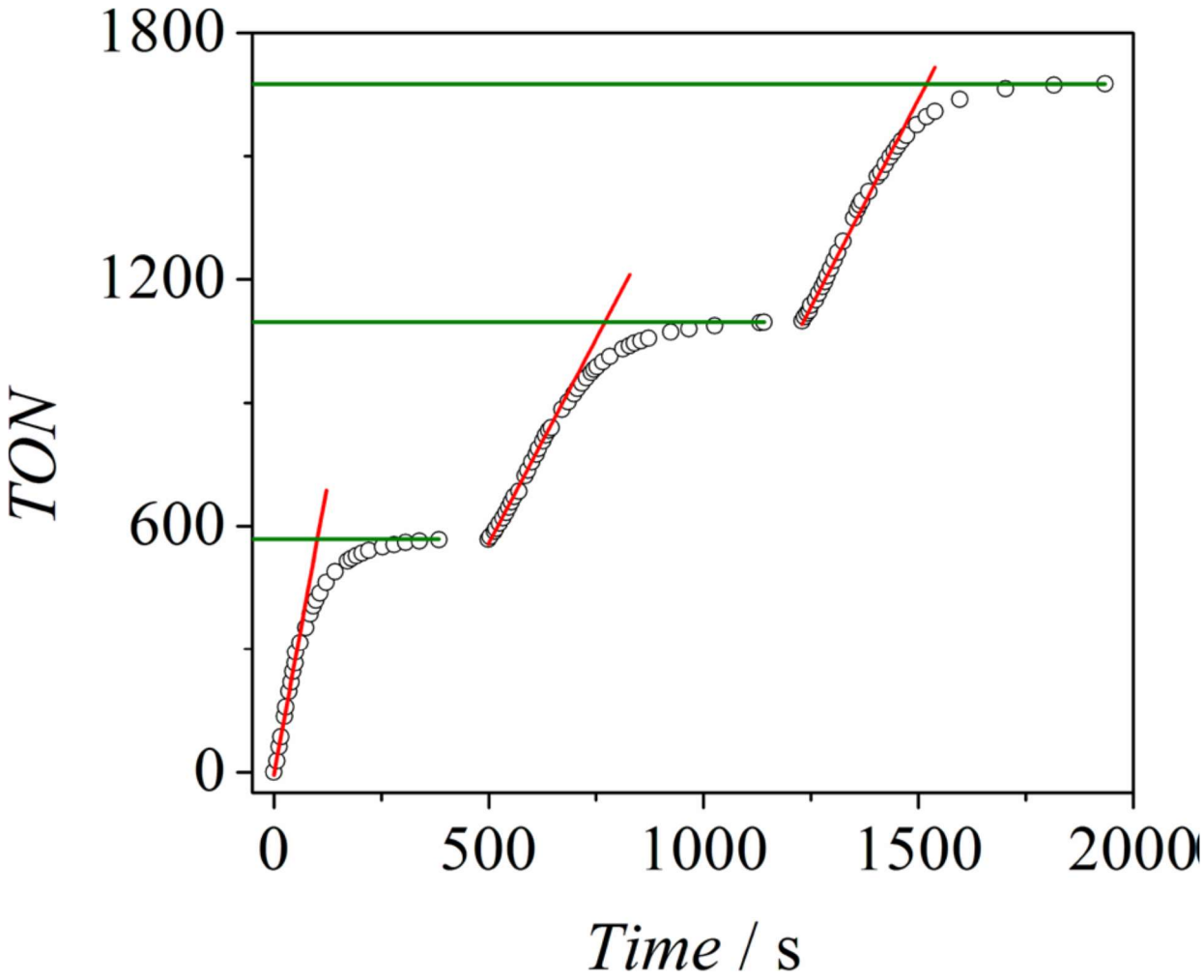

962
963
964
965

FIGURE 13

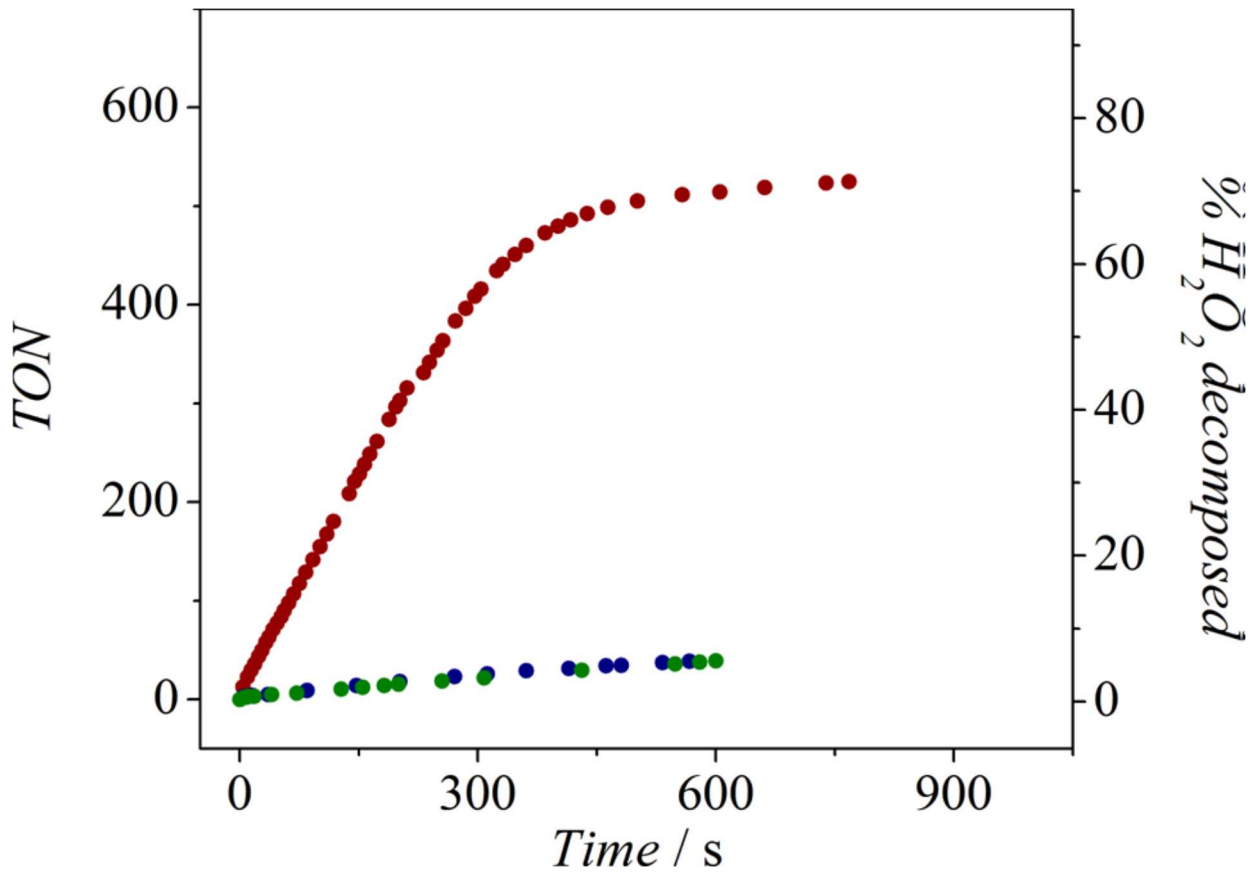
600
400
200
0
TON
80
60
40
20
0
% H_2O_2 decomposed
0
300
600
900
Time / s

Table 1. Crystal Data and Structure Refinement for Compounds 1 and 2)

	1·H_2O·0.5 CH_3CN	2·CH_3CN
formula	$C_{148}H_{142}Mn_8N_{16}O_{40}$[a]	$C_{36}H_{33}Cl_2Mn_2N_5O_{16}$
Fw (g/mol)	3670.28	998.49
crystal color, habit	green, needle	green, needle
T (K)	100(2)	100(2)
λ (Mo Kα), Å	0.71073	0.71073
crystal size (mm)	0.65 × 0.26 × 0.21	0.57 × 0.07 × 0.02
crystal system	monoclinic	monoclinic
space group	$C2/c$	$P21/c$
a, Å	16.3701(6)	17.826(7)
b, Å	24.5812(9)	21.265(7)
c, Å	9.9600(4)	10.759(4)
β, deg	99.328(1)	95.72(1)
V, Å^3	3954.9(3)	4058(2)
Z	1	4
ρ_{calcd}, g·cm^{-3}	1.541	1.631
μ, mm^{-1}	0.718	0.835
$F(000)$	1878	2032
θ range, deg	2.39 to 25.08	1.15 to 20.81
completeness to θ = 25.10°	99.8%	99.5%
index ranges	h = −19 → 19	h = −17 → 17
	k = −29 → 29	k = 0 → 21
	l = −11 → 11	l = 0 → 10
data/restraints/parameters	3515/106/306	4226/1/562
GOF on F^2	1.110	0.824
R_1[b], wR_2[c] [$I > 2\sigma(I)$]	0.0507, 0.1515	0.0352, 0.0768
R_1[b], wR_2[c] (all data)	0.0520, 0.1525	0.0914, 0.0966

[a] 4 equiv of 1·H_2O·0.5CH_3CN. [b] $R_1 = \sum||F_o| - |F_c||/\sum|F_o|$. [c] $wR_2 = \{\sum[w(F_o^2 - F_c^2)^2]/\sum[w(F_o^2)^2]\}^{1/2}$, $w = 1/[\sigma^2(F_o^2) + (aP)^2 + bP]$, where $P = [\max(F_o^2, 0) + 2F_c^2]/3$.

Table 2 Selected Interatomic Distances (Å) and Angles (deg) for Compound 1a

Mn1–O1	1.782(1)
Mn1–O2	1.970(2)
Mn1–O3	2.167(2)
Mn1–O5/Mn1′–O6′	2.200(3)
Mn1–N1	2.067(3)
Mn1–N2	2.064(3)
Mn1···Mn1′	3.1412(9)
Mn1–O1–Mn1′	123.5(2)
O1–Mn1–N2	168.48(9)
O2–Mn1–N1	170.3(1)
O3–Mn1–O5	174.7(1)
O5–Mn1···Mn1′–O6′	78.1(1)
O3–C11–C12–C13	36.2(5)

[a]Standard deviations in parentheses. Symmetry codes: (′) 1 − *x*, *y*, 1.5 − *z*.

Table 3. Selected Interatomic Distances (Å) and Angles (deg) for Compound 2a

Mn1–O1	1.784(4)	Mn2–O1	1.791(4)
Mn1–O3	1.965(4)	Mn2–O6	1.956(4)
Mn1–N2	2.056(5)	Mn2–N3	2.050(5)
Mn1–N1	2.060(5)	Mn2–N4	2.054(5)
Mn1–O5	2.177(4)	Mn2–O2	2.120(4)
Mn1–O8	2.219(4)	Mn2–O9	2.300(4)
O3–Mn1–N2	170.6(2)	O6–Mn2–N3	166.5(2)
O1–Mn1–N1	166.7(2)	O1–Mn2–N4	169.2(2)
O5–Mn1–O8	170.8(2)	O2–Mn2–O9	171.1(2)
Mn1–Mn2	3.139(2)	O5–C29–C30–C35	50.3(9)
Mn1–O1–Mn2	122.8(2)	O2–C21–C22–C27	8(1)
O8–Mn1–Mn2–O9	95.2(2)		

[a]Standard deviations in parentheses.

Table 4. Textural Properties of Materials SiO2−CTA, SiO2−Ex, SiO2−TMA, and [Mn2O]@SiO2

	SiO_2-CTA	SiO_2-Ex	SiO_2-TMA	$[Mn_2O]@SiO_2$ from 1	$[Mn_2O]@SiO_2$ from 2
d_{100}, nm	4.1		4.1	4.1	4.1
a_0,[a] nm	4.7		4.8	4.7	4.8
intensity,[b] 1×10^3 counts	100		230	139	119
HWHH[c] 2θ, deg	0.24		0.23	0.27	0.28
BET surface area, $m^2\ g^{-1}$		945			
C		102	73	53	50
porous volume, mL g^{-1}		0.80	0.69	0.36	0.36
pore diameter,[d] nm		3.8	3.7	2.8−3.4	2.8−3.3

[a]Parameter calculated from d_{100} with the formula $a_0 = 2d_{100}/3^{1/2}$. [b]Height at the maximum of (100) peak. [c]Half-width at half-height. [d]Using BdB method.

Table 5. Summary of Catalytic Results for Compounds 1 and 2 with [H2O2]0 = 1.05 M and [MnIII2] = 0.8 mM in CH3CN−H2O 9:1 (v/v)

	at 1 min		at 2 min		at 10 min	
sample	TON[a]	% H_2O_2[b]	TON[a]	% H_2O_2[b]	TON[a]	% H_2O_2[b]
1	227	31	334	46	515	70
2	182	25	257	35	437	60

[a]TON = mmol O_2/mmol Mn^{III}_2. [b]% H_2O_2 decomposed.

Table 6. Summary of Catalytic Results for Compounds 1 and 2 and Material [Mn2O]@SiO2 with [H2O2]0 = 1.05 M and [MnIII2]= 0.8 mM in CH3CN−H2O 9:1 (v/v)

sample	pH	at 1 min		at 2 min		at 10 min	
		TON[a]	% H_2O_2[b]	TON[a]	% H_2O_2[b]	TON[a]	% H_2O_2[b]
$[Mn_2O]@SiO_2$	8.9	312	42	440	60	587	80
1	6.0	227	31	334	46	515	70
2	6.0	182	25	257	35	437	60
2	7.3	295	40	366	50	514	70
2	9.8	374	51	496	67	582	79

[a]TON = mmol O_2/mmol Mn^{III}_2. [b]% H_2O_2 decomposed.

Table 7. Summary of Catalytic Results for Compounds 1 and 2 and Material [Mn2O]@SiO2 with [H2O2]0 = 1.05 M and [MnIII2]= 0.8 mM in Water

sample	at 1 min		at 2 min		at 10 min	
	TON[a]	% H_2O_2[b]	TON[a]	% H_2O_2[b]	TON[a]	% H_2O_2[b]
$[Mn_2O]@SiO_2$	98	13	180	25	514	70
1	7	1	12	2	39	5
2	6	1	10	1	39	5

[a]TON = mmol O_2/mmol Mn^{III}_2. [b]% H_2O_2 decomposed.

1031 **Table 8.** Summary of Properties for Material [Mn2O]@SiO2 and Post-Catalysis Products

1032

Table 8. Summary of Properties for Material $[Mn_2O]@SiO_2$ and Post-Catalysis Products

sample	mesostructure	porous volume, $cm^3 \cdot g^{-1}$	% mass loss[a]
$[Mn_2O]@SiO_2$	yes	0.36	21.9
$[Mn_2O]@SiO_2^{4h}$	yes	0.58	7.4
$[Mn_2O]@SiO_2^{4hr}$	no		
$[Mn_2O]@SiO_2^{4hl}$	yes	0.50	9.1

[a]Loss of the Mn complex's ligands in the range of 200−400 °C, according to TGA.

1033

1034

1035